Ultrafast Charge Transfer and Coherent Phonons in Electroactive Organic Cation-Templated Low-Dimensional Perovskite Analogues

Ilan Devroey[1,2†], Yorrick Boeije[3,4†], Peter Banks[5], Claudio Quarti[5], Paola La Magna[6], Aleksandra Ciesielska[1,2], Laurence Lutsen[2,7], Elien Derveaux[7,8], Peter Adriaensens[7,8], Kristof Van Hecke[6], David Beljonne[5], Samuel D. Stranks*[3,4], Wouter T. M. Van Gompel*[1,2,7]

1 Hasselt University, Institute for Materials Research (imo-imomec), Hybrid Materials Design (HyMaD), Martelarenlaan 42, B-3500 Hasselt, Belgium.

2 Energyville, imo-imomec, Thor Park 8320, B-3600, Genk, Belgium.

3 University of Cambridge, Department of Chemical Engineering and Biotechnology, Cambridge, UK.

4 University of Cambridge, Department of Physics, Cavendish Laboratory, Cambridge, UK.

5 University of Mons, Laboratory for Chemistry of Novel Materials, Materials Research Institute, Place du Parc 20, B-7000 Mons, Belgium.

6 Ghent University, Department of Chemistry, XStruct, Krijgslaan 281-S3, B-9000 Ghent, Belgium.

7 imec, imo-imomec, Wetenschapspark 1, B-3590, Diepenbeek, Belgium

8 Hasselt University, Institute for Materials Research (imo-imomec), Applied and Analytical Chemistry, NMR group, Martelarenlaan 42, B-3500 Hasselt, Belgium.

Abstract

Hybrid organic-inorganic perovskites (HOIPs) have emerged as promising materials for optoelectronic applications, yet gaining control over their structural and electronic tunability remains a key challenge. In this study, we introduce 7H-dibenzo[*c*,*g*]carbazole (DBCz) as a novel electroactive organic cation that enables the formation of two distinct low-dimensional hybrid metal halides: a conventional 2D perovskite structure, $(DBCz)_2PbI_4$, and a previously unreported layered perovskite analogue structure with edge-sharing octahedra, $DBCzPbI_3$. The edge-sharing phase represents a new structural motif within the hybrid metal halide family. Both materials exhibit a type-II band alignment, facilitating ultrafast photoinduced hole transfer from the inorganic to the organic layer. Using transient absorption spectroscopy, we identify the formation of DBCz-based hole polarons in both phases, and uniquely observe the charge-transfer-induced formation of triplet states and room-temperature coherent phonons for the perovskite analogue phase. These findings highlight the role of molecular design in controlling excited-state dynamics and exciton–lattice interactions in hybrid metal halides.

Introduction

Hybrid organic-inorganic perovskites (HOIPs) are currently in the spotlight for optoelectronic applications, such as solar cells, photodetectors, lasers, and LEDs.[1-4] In recent years, the interest in the sub-class of 2D layered HOIPs has increased due to their inherently enhanced environmental stability, as compared to their 3D analogues, and their high structural and compositional flexibility.[3] The organic ammonium cation used for the formation of 2D HOIPs can be selected from a large potential pool of molecules.[5] In most cases, the organic cation does not directly contribute to the optical or electronic properties of the hybrid.[6-8] In contrast, the use of so-called electroactive organic cations has recently gained prominence.[7, 8] When commonly used organic cations, such as butylammonium (BA) or phenylethylammonium (PEA), are incorporated, a type-I electronic level alignment is obtained between the organic and inorganic components (*i.e*. the frontier energy levels of the organic cation are far removed from the band edges of the inorganic framework).

In such a case, the charge carriers are confined within the inorganic framework. With proper molecular design, electroactive organic cations can result in the formation of a type-II band alignment, one of the levels of the organic intercalating within the band gap of the inorganic frame. Over the years, a number of studies have explored the use of electroactive organic cations in order to tune properties such as charge transfer, energy transfer, exciton binding energy, and charge transport.[7] Examples include carbazole (Cz)[6, 9-14], pyrene[15-21], oligothiophene derivatives[22-26], tetrazine[27], and naphthalenediimide[28-31].

Carbazole (Cz) is one of the more prominent organic cores used as an electroactive organic cation,[6, 9-14] which has also been shown to significantly enhance the environmental stability of the resulting 2D HOIP.[6, 10, 11] Previous work has demonstrated that electronic coupling occurs between the carbazole layer and the inorganic layer, with the formation of an organic-inorganic charge-transfer state, and that the out-of-plane mobility is enhanced for thin films of Cz-containing 2D HOIPs in comparison to a PEA-containing 2D HOIP.[6] However, to the best of our knowledge, the crystal structure of a hybrid metal halide compound containing a carbazole derivative has not been reported yet despite intensive efforts. This comparative lack of structural insights complicates the formulation of detailed structure-property relationships. The growth of single crystals (SCs) is generally required to obtain the crystal structure *via* single-crystal X-ray diffraction. To tackle this challenge, we hypothesized that structurally modifying Cz *via* the extension of the conjugated system to obtain 7H-dibenzo[*c,g*]carbazole (DBCz), should alter the weak interactions between the molecules as well as modify their solubility in polar aprotic solvents so as to potentially facilitate crystal growth while maintaining the desired type-II band alignment.

In this work we show that besides the typical 2D HOIP with an A_2PbI_4 stoichiometry, another low-dimensional phase with $APbI_3$ stoichiometry can also be selectively obtained selectively in polycrystalline thin films of lead iodide–based hybrid metal halides containing an electroactive DBCz organic cation. Single crystals of the $APbI_3$ phase were successfully grown, and the crystal structure was resolved. The resulting crystal structure is that of a hybrid material with 2D metal halide layers consisting of distorted edge-sharing octahedra in a corrugated network separated by a bilayer of the DBCz organic cations. To the best of our knowledge, no metal halide framework (MHF) with the same octahedral connectivity has been reported in the literature so far (based on the CCDC database). As the MHF does not consist of metal halide octahedra connected to 4 neighbors *via* corner-sharing and is solely connected to its neighbors *via* an edge-sharing pattern, the compound is not a 2D perovskite, but it can be classified broadly as a hybrid metal halide or more specifically as a perovskite analogue.[32-35] We present a detailed study of the optical properties of the lead iodide-based hybrid metal halides containing an electroactive DBCz organic cation, based on steady-state absorption and emission spectroscopy, as well as transient absorption spectroscopy. Similar to the Cz 2D perovskite,[6] both the 2D perovskite ($(DBCz)_2PbI_4$) as well as the perovskite analogue ($DBCzPbI_3$) containing the DBCz cation show clear indications of photoinduced hole-transfer from the inorganic framework to the organic cation. Despite the similar initial ultrafast charge transfer, the crystal structure has a pronounced effect on the subsequent carrier recombination dynamics and exciton–phonon coupling. Photoinduced charge transfer leads to the formation of triplets localized on DBCz only in $DBCzPbI_3$, but not in $(DBCz)_2PbI_4$. Finally, the unique edge-sharing lead-halide octahedral connectivity in $DBCzPbI_3$ gives rise to a substantial Herzberg–Teller type exciton–phonon coupling, as revealed by picosecond room-temperature phonon coherences.

Results and discussion

The synthesis of the DBCz-based alkyl ammonium salt is described in detail in the Supplementary Information. In our previous work, the synthesis of Cz-based alkyl ammonium salts was reported, and

the same 4-step synthesis route (alkylation, Gabriel synthesis, salt formation) was used to synthesize DBCz-C5-NH_3I, abbreviated as DBCzI (Scheme 1).[10]

We selected the longest alkyl tail length that was previously used for Cz,[6] a length of 5 CH_2 groups (C5), due to the bulkiness of the DBCz core.

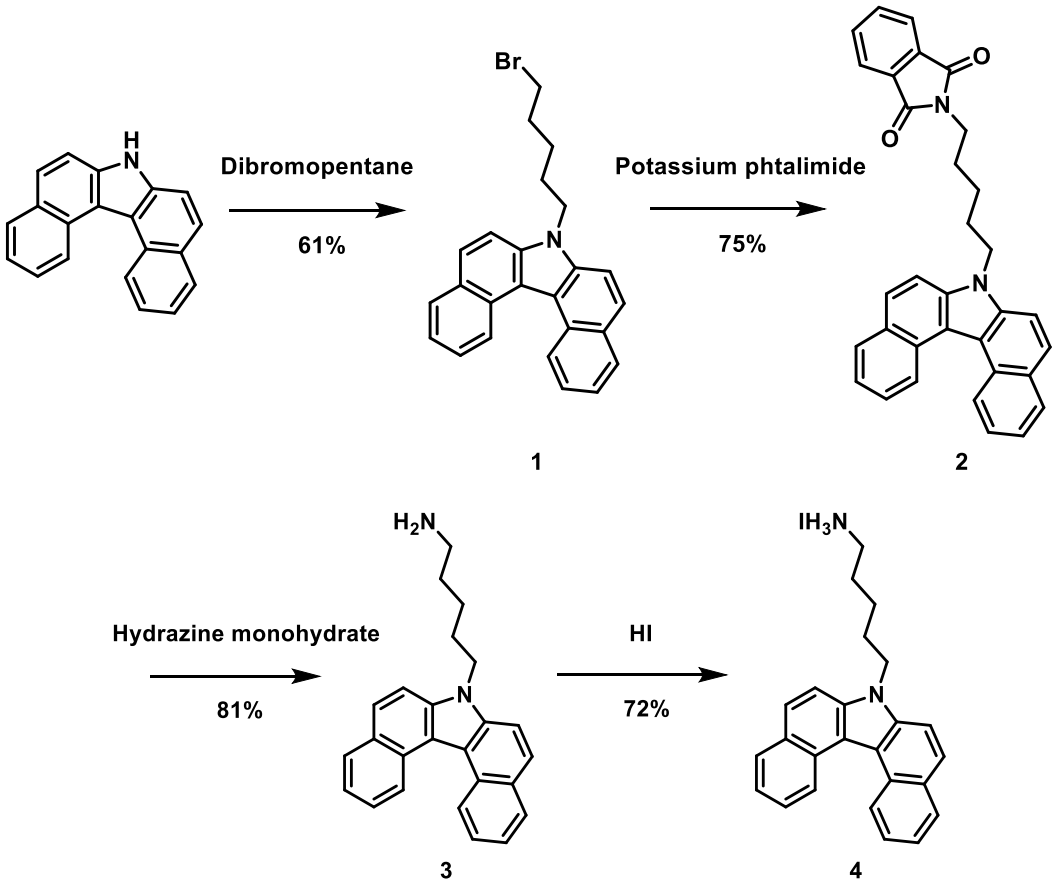

Scheme 1. Synthesis route to obtain the DBCz-based ammonium iodide salt.

To demonstrate that the structural modification of carbazole results in altered weak interactions between the molecules, we attempted to grow single crystals. A crystal growth technique based on anti-solvent vapor diffusion[36-38] was used (described in detail in the SI), resulting in the formation of thin yellow platelets. As we initially postulated, the structural modification of Cz with two additional benzene rings has a significant impact on the solubility in gamma butyrolactone. A simple solubility experiment showed that the solubility limit of the precursor was more than halved when DBCz is used in comparison to a Cz-based precursor solution (Table S2). Upon structure resolution, it becomes apparent that the crystal structure of this novel DBCz-based compound is markedly different from that of a regular 2D HOIP. The obtained crystal structure shows a 2D layered structure (Fig. 1b, 1c), but it does not have the characteristic corner-sharing octahedra connectivity, typical of a 2D HOIP.[5] Instead, the inorganic network consists of a 2D corrugated framework built up out of dimers of edge-sharing distorted PbI_6 octahedra (Fig. 1b). The ammonium head groups of the DBCz cations penetrate into the cavities created by 6 connected edge-sharing octahedra, forming hydrogen bonds with the iodide atoms of three of these octahedra (Fig. S1a). The stoichiometry also differs from that of a 2D HOIP, as the structural formula of this phase is ABX_3. For these reasons, this material can be categorized under the family of low dimensional perovskite analogues. To further highlight the unique distortion characteristics of the new material, we have calculated the average bond length distortion (Δd) and the average bond angle variance (σ^2) according to the formulas provided by Mitzi *et al.*[39] Values of 139.54

10^{-5} and 201.7 are found for Δd and σ^2, respectively. In comparison to other typical corner-shared octahedral lead-iodide-based 2D HOIPs, these values are significantly higher, indicating a pronounced structural distortion (Fig. S2 and S3).

Despite our best efforts and the utilization of different crystal growth methods, we have been unable to obtain crystals of any other phase besides this edge-sharing phase. With the intention of studying the impact of the novel arrangement of the inorganic network on the photophysical properties in comparison to the more common 2D HOIP inorganic framework, we attempted to exert influence over the formation process of both compounds in the form of thin films.

We found that, *via* spincoating, we were able to control the formation process. We were able to selectively synthesize $(DBCz)_2PbI_4$ thin films as well as $DBCzPbI_3$ thin films (Fig. S4). More specifically, while varying the precursor stoichiometry (DBCzI to PbI_2 ratio) did not yield different results during the crystal growth process, always forming the edge-sharing phase, tuning the precursor stoichiometry is crucial to obtain phase-pure thin films *via* spin-coating. We hypothesize that the preferential formation of crystals of $DBCzPbI_3$ over those of $(DBCz)_2PbI_4$ through various crystal growth methods is related to the very bulky DBCz molecules, which expectedly put a lot of strain on a 2D framework of a fully corner-sharing inorganic framework.[40] The possibility of forming a 2D HOIP *via* thin film processing, while a different phase is consistently formed in single crystal growth experiments using the same organic cation, has been previously reported in the literature.[37, 41] While spin coating is a very rapid deposition and crystallization process that even allows for the formation of kinetic products, crystal growth is a comparatively much slower process that generally favors the formation of the thermodynamically preferred product.[42]

The synthesis of $(DBCz)_2PbI_4$ and $DBCzPbI_3$ thin films was achieved by spincoating the precursor solution comprising stoichiometric ratios of DBCzI and PbI_2 onto quartz substrates. In order to obtain phase-pure thin films of both phases, regular hot-plate annealing did not suffice, and a combination of hot-plate and solvent vapor annealing with DMSO was required (Fig. S5).[43] The detailed procedure is described in the SI. As reported before by some of the authors for a 2D HOIP containing a benzothienobenzothiophene (BTBT) derivative as the organic cation, the DMSO solvent vapor is hypothesized to increase the mobility of the ions—and especially that of the bulky organic cation—during the annealing procedure which is required for the formation of a highly crystalline thin film with such a bulky organic cation. When a 2:1 ratio of DBCzI/PbI_2 in the precursor was used with the optimal processing conditions (Table S1), the UV-vis absorption spectrum shows an excitonic peak at 505 nm (Fig. 1d), which is characteristic for a 2D lead iodide HOIP.[38, 44] The diffraction pattern of the corresponding thin film reveals a series of equally spaced reflections typical for thin films of 2D HOIPs with a strong preferential horizontal orientation.[44] An interplanar spacing of 29.2 Å is obtained (Fig. 1e), which is close to the length of two fully extended DBCzI molecules (28.4 Å), indicating the presence of a typical bilayer of organic cations in between the inorganic layers.

When spincoating a precursor solution with DBCzI and PbI_2 in a 1:1 molar ratio, to obtain an ABX_3 stoichiometry, thin films of the corresponding edge-sharing phase could also be obtained when solvent vapor annealing with DMSO was applied (Table S1, Fig. S6). In the absorption spectrum, the excitonic peak of $DBCzPbI_3$ appears at a shorter wavelength (399 nm/3.1 eV) compared to $(DBCz)_2PbI_4$ (505 nm/2.45 eV). As the absorption peak of the DBCz π-conjugated spacer lies at 375 nm (see Fig. 1d), the 399 nm signal from $DBCzPbI_3$ can be safely associated with the lead-iodide frame. It is blue shifted by 0.65 eV compared to the 2D HOIP frame, reflecting changes in the lead-iodide octahedral connectivity. Indeed, it has been shown in the literature that a lead iodide framework with edge-sharing octahedra results in a wider bandgap than an equivalent corner-sharing framework.[45] In the XRD pattern, there is a clear shift of the reflections to a higher 2θ value (Fig. 1e). An interplanar spacing of

22.0 Å is obtained. This smaller interplanar spacing is corroborated by the crystal structure of $DBCzPbI_3$, as the organic cations are stacked in a sideways manner (Fig. S1b), differing from the typical bilayer that is expected for the 2D HOIP.

We observe strongly quenched photoluminescence for $(DBCz)_2PbI_4$ as well as $DBCzPbI_3$ (Fig. 1d) thin films. Whereas in both phases the Wannier exciton emission localized on the PbI-framework is fully quenched, a broad red emission band is observed for $DBCzPbI_3$, which overlaps with the red shoulder in the DBCzI salt emission spectrum (500–800 nm). We will revisit the assignment of this emission band at a later stage.

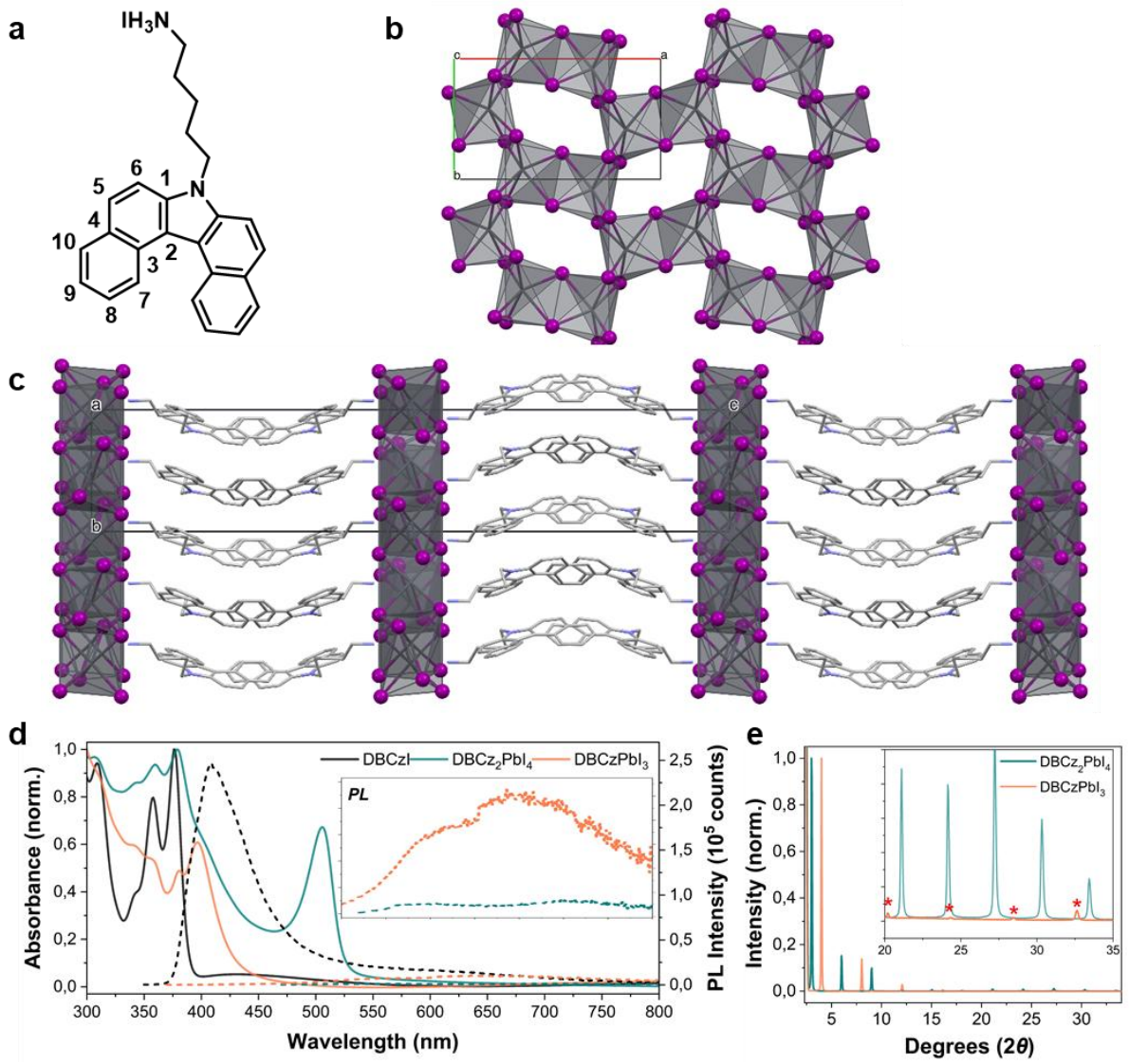

Figure 1. (a) Molecular structure of DBCzI with numbering of the carbon atoms of the DBCz core. (b and c) Crystal structure of $DBCzPbI_3$ without H-atoms and without positional disorder of the alkyl chains (for clarity) with the packing down the c-axis and the a-axis, respectively. (d) Normalized UV-Vis absorption spectra (solid lines) and PL spectra (dashed lines) of thin films of the DBCz-based ammonium iodide salt (black), $(DBCz)_2PbI_4$ (blue) and $DBCzPbI_3$ (orange). PL spectra were collected at room temperature after excitation at 300 nm, 350 nm, and 350 nm, respectively. The inset contains a zoom-in of the PL spectra of $(DBCz)_2PbI_4$ and $DBCzPbI_3$ between 450 and 800 nm. (e) Normalized XRD

patterns of the thin films of $(DBCz)_2PbI_4$ (blue) and $DBCzPbI_3$ (red). The structural features of $DBCzPbI_3$ are highlighted with a red asterisk in the inset.

Electronic level alignment

Earlier work indicated that a Cz-based 2D HOIP possesses a type II electronic alignment. Specifically, the HOMO level of carbazole lies above the valence band maximum of its corresponding inorganic perovskite framework.[6] With the aim of comparing the energy levels of DBCz with those of Cz and verifying that the alignment relative to that of a typical 2D lead iodide perovskite inorganic framework remains unchanged, cyclic voltammetry (CV) was utilized. Note that CV measurements directly on the ammonium iodide salts are not reliable due to interference from the redox reactions of the iodide anion.[22] To determine reliable oxidation and reduction potentials of the DBCz and Cz organic cores, the nitrogen atoms of both molecules were protected with a propyl group since unsubstituted nitrogen atoms are sensitive to oxidation.[46]

Furthermore, the presence of an alkyl chain also ensures decent solubility without significantly influencing the energy levels. The HOMO levels of Cz and DBCz were determined to be -5.69 and -5.60 eV respectively (Fig. S7, Table S4), indicating that the extension of the conjugated system has a minor influence on the position of the HOMO level. We note that the optical bandgap shrinks from 3.51 eV for Cz to 3.28 eV for DBCz, so the extension of the conjugated system mainly affects the LUMO level for these molecules. Therefore, given the higher HOMO energy of DBCz relative to Cz, $(DBCz)_2PbI_4$ is expected to exhibit a type II band alignment, similar to that of $(Cz\text{-}C_x)_2PbI_4$.

Due to difficulty in obtaining single crystals of $(DBCz)_2PbI_4$ suitable for single-crystal X-ray diffraction experiments, we employ a computational approach to investigate the structural properties of this system. Using periodic density functional theory (DFT), performed at the PBE-D3/pobTZVP level using Stuttgart small-core effective core pseudo-potentials for lead and iodine atoms, we obtain a structural model exhibiting a PXRD pattern in good agreement with what is observed experimentally, as illustrated in Fig. S8.[47-49] As shown in Fig. S9, the organic ligands of $(DBCz)_2PbI_4$ exhibit a more upright orientation in the obtained optimized crystal structure than the perovskite analogue $DBCzPbI_3$ system, consistent with the expectations for the bilayer of the 2D phase. Further examination of the electronic structure for this model (*vide infra*) confirms that the $(DBCz)_2PbI_4$ system studied here exhibits a type II alignment of the electronic states (Fig. S10).

While the alignment of corner-sharing 2D HOIP systems has been studied in detail in the literature, there exists no such clear precedent for 2D hybrid perovskite analogue systems with an edge-sharing motif.[50] Thus, to further elucidate the energetic alignment, we performed periodic DFT calculations for $DBCzPbI_3$, using the hybrid PBE0 potential for the description of the exchange and correlation energy, with 30% HF exchange energy, together with Spin-Orbit Coupling (SOC) corrections. Though a recent work points out the importance of properly accounting for the different dielectric screening in the inorganic and organic components to model the electronic properties of 2D halide perovskites,[51] the present level of theory was shown to satisfactorily predict the electronic band gap of 2D HOIPs, in the presence of electronically inert spacers.[52] For $DBCzPbI_3$, we indeed find a type II alignment, with an offset between the molecular HOMO and inorganic valence band maximum (VBM) of 0.92 eV, as well as an offset of the molecular LUMO and inorganic conduction band minimum (CBM) of 1.40 eV, as depicted in Fig. 2. Our calculations predict a single particle electron band gap for $DBCzPbI_3$ of 3.9 eV, which is consistent (though likely overestimated by the DFT calculation) with the 3.1 eV optical band gap measured experimentally accounting for excitonic effects, with exciton binding energies which can amount to 0.5 eV in 2D and 1D HOIPs.[53 54]

Interestingly, the calculations point out that the frontier electronic states are pure states of the inorganic or organic frame. In other words, no state mixing is observed in the $DBCzPbI_3$ case, in contrast, for instance, to recent findings for 2D HOIPs incorporating pyrene derivatives as spacers.[21] The band structure of $DBCzPbI_3$ (computed at the PBE+SOC level due to the computational limitations for a unit cell with a large amount of atoms), reveals an indirect band gap for the inorganic frame, with the CBM located at Γ, and the VBM located in the middle of the $\Gamma \rightarrow$Y path (Fig. S11). On the other hand, as the bands are rather flat, the lowest energy direct transition falls at Γ and is only 0.1 eV higher in energy. Furthermore, group-theory based symmetry analysis reveals that this lowest-energy VBM→CBM direct transition at Γ is symmetry-forbidden (Supplementary Note 1). However, a bright direct VBM→CBM+1 transition is also present, which lies only 40 meV above the dark one and dominates the optical absorption.

Type II band alignment may lead to photoinduced charge transfer, which reduces the radiative decay probability of excitons, due to potential spatial separation of the electron and hole. This is consistent with the strongly quenched photoluminescence in $(DBCz)_2PbI_4$ as well as $DBCzPbI_3$ (Fig. 1d), reminiscent of the Cz-based 2D perovskite $(Cz\text{-}C_3)_2PbI_4$ in earlier work.[6]

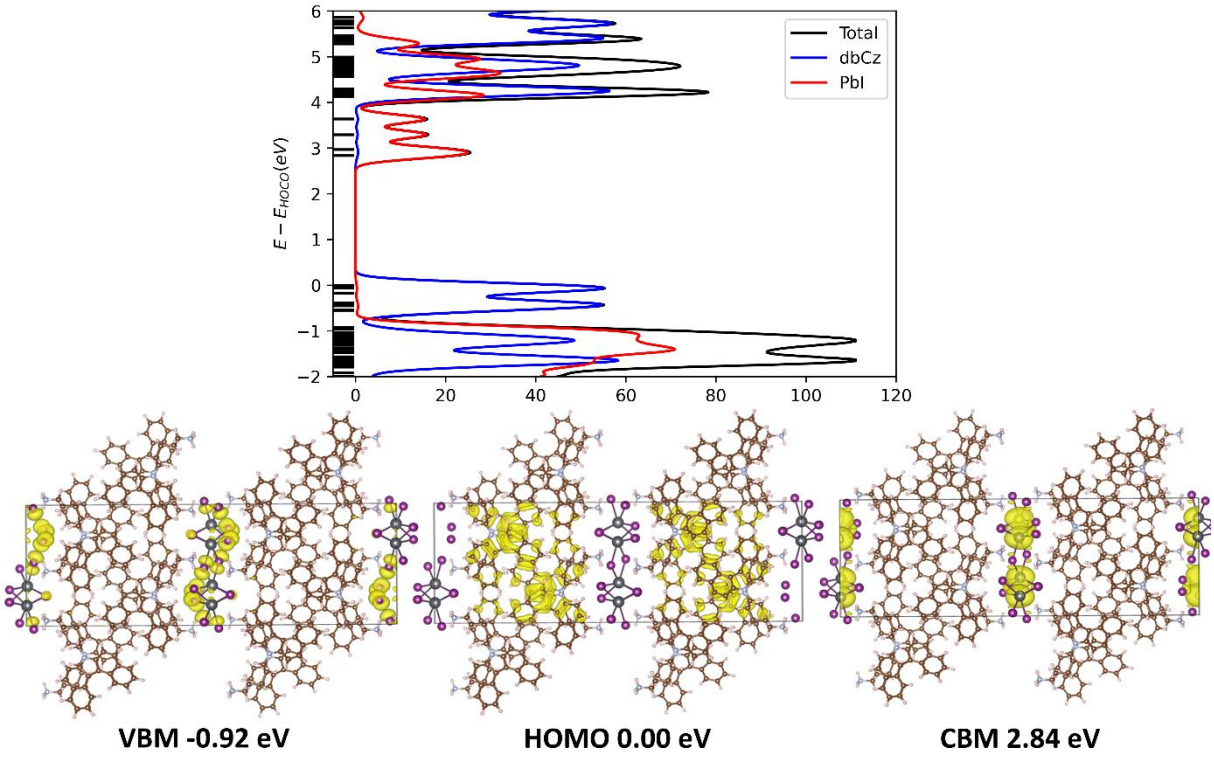

Figure 2. Projected density of states for $DBCzPbI_3$ (top) and electronic isosurfaces of the valence band, HOMO, and conduction band (bottom), calculated at the PBE0+SOC level of theory, including 30% HF exchange energy. Contributions from organic and inorganic components are illustrated with blue and red traces, respectively, while the total density of states is visualized in black. Discrete electronic states are visualized as black bars. Band energies are normalized to the system highest occupied crystalline orbital (HOCO).

Photoinduced charge transfer

We turn to transient absorption (TA) spectroscopy to explore photoinduced charge transfer and recombination mechanisms in both phases. TA spectroscopy does not rely on bright emitting species, since the optical pump-induced changes in absorption are probed. We start our discussion with the 2D

HOIP, $DBCz_2PbI_4$. Photoinduced charge transfer, favored by the energetic alignment (*vide supra*) is expected to result in the formation of polaronic species on the organic layer (which can be described as radical cations) with a characteristic absorption profile. With a 490 nm pump, the PbI_4^{2-} sublattice is selectively excited—from here on loosely referred to as PbI*—without any contribution from direct DBCz absorption (Fig. S12). The PbI* ground-state bleach (GSB, positive $\Delta T/T$) centered around the band edge (500 nm) is commonly observed for 2D HOIPs. The bleach feature is sandwiched by two perovskite-inherent photoinduced absorption (PIA) features that have been associated with hot carrier cooling and band-gap renormalization.[55] Next to these features that are expected for any 2D HOIP, a broad photoinduced absorption (PIA, negative $\Delta T/T$) appears around 600–850 nm (Fig. 3a and 3b).

Based on the spectral similarity to the propyl-DBCz hole polaron absorption spectrum measured by oxidising propyl-DBCz in DCM with $FeCl_3$ (black line),[11] we assign this broad PIA to the DBCz radical cation ($DBCz^{+\cdot}$) absorption formed through ultrafast (<200 fs; below the temporal resolution of our instrument) hole transfer from PbI*. The hole polaron spectrum in solution (Fig. S13) also reveals a strong absorption peak at 485 nm, which is outside of our TA probe range. However, the strong PIA at 470 nm might still have contributions from this $DBCz^{+\cdot}$ transition. The DBCz GSB is observed between 375–410 nm due to charge-transfer-induced depopulation of the DBCz ground-state.

The differences between the hole polaron absorption bands of the oxidized solution propyl-DBCz and photoexcited $DBCz_2PbI_4$ can reasonably be ascribed to differences in the environment (dielectric constant) and the packing of the DBCz molecules inside the organic layer of the hybrid (solid state) compared to the solution. Additional NMR measurements confirm that in solution, the hole polaron is formed after oxidation without structural changes or without the formation of new side products (Fig. S14).[56] Furthermore, we uncover that the hole polaron is mainly localized on the position labeled as 5 (and the identical position on the other half of the π-system, due to the symmetrical nature of the molecule) in Fig. 1a (Fig. S14, S15). More details about the oxidation and the NMR experiments can be found in the supporting information. Finally, we note that the $DBCz^{+\cdot}$ PIA feature is broader than previously observed for $Cz^{+\cdot}$,[6] expectedly due to enhanced delocalization of the positive charge.

Both the VIS and UV picosecond TA spectra are substantially different from the spectra of the organic ammonium iodide salt DBCzI (also plotted in Fig. 3b), confirming our assignment of the observed PIA signals to $DBCz^{+\cdot}$ generated by charge transfer with the inorganic framework rather than DBCz* generated directly *via* energy transfer.

While no rise can be resolved in the PIA signal following 490-nm excitation—indicating the inorganic-to-organic hole transfer process is ultrafast (<200 fs)—a small rise component of ~7 ps in the PbI GSB and ~0.7 ps in the $DBCz^{+\cdot}$ PIA is observed upon 400-nm excitation (Fig. S16), suggesting a slower organic-to-inorganic electron transfer[29, 57] from the small fraction of excited DBCz molecules (Fig. S12). The discrepancy between the GSB and PIA rise times may partially reflect hot carrier cooling, although the ~7 ps timescale is notably long compared to typical lead halide perovskites, suggesting a possible hot phonon bottleneck.[58] In this case, the rise kinetics in both the GSB and PIA features could reflect delayed hole transfer from photoexcited PbI* to DBCz, mediated by retarded hot carrier cooling.

The DBCz-localized hole polarons ($DBCz^{+\cdot}$) and PbI-localized electrons formed through charge transfer have almost fully decayed after 7 ns (Fig. 3c). Their overlapping normalized kinetics indicate that their decay mechanisms are coupled. Together with the absence of any PL (Fig. 1d), we conclude that these electron and hole polarons recombine non-radiatively on a few ns timescale. The absence of any fluence dependence further suggests that geminate recombination of a bound charge transfer state dominates the decay (Fig. S17).

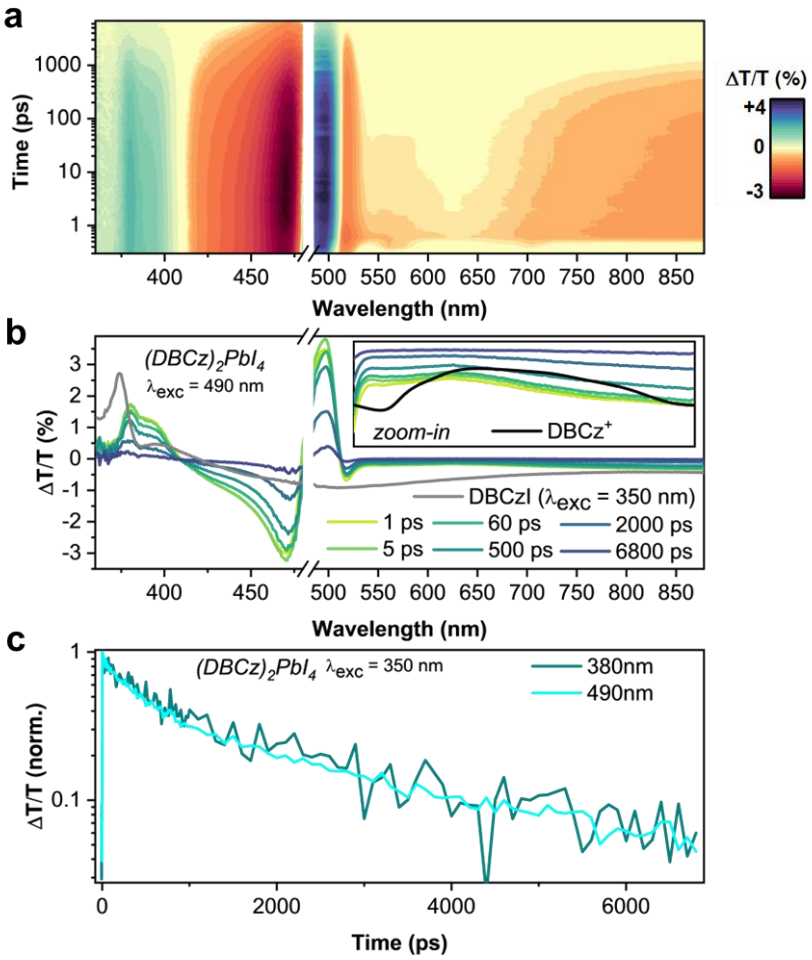

Figure 3. (a) Stitched UV and VIS transient absorption (TA) maps of a $(DBCz)_2PbI_4$ thin film photoexcited at 490 nm. A small spectral gap around 480—485 nm appears where the noise floor for both probes is relatively high. Note that the pump scatter at 490 nm overlaps with the PbI ground state bleach. (b) Stitched UV and VIS TA spectra. The DBCzI salt TA spectrum at 1 ps, photoexcited at 350 nm, is shown in grey. The inset shows zoomed-in spectra between 525 and 880 nm. The DBCz hole polaron spectrum, measured in solution (Fig. S13), is overlaid in black. (c) Normalized kinetics probed at 380 nm and 490 nm, representing DBCz and PbI decay, respectively. The kinetics are plotted for an excitation wavelength of 350 nm to remove the pump scatter contribution.

The TA maps, spectra and kinetics are shown in Fig. 4 for $DBCzPbI_3$. Contrary to the case of $(DBCz)_2PbI_4$, selective excitation of either the PbI sublattice or DBCz is not possible for $DBCzPbI_3$, as the absorption spectra of the inorganic and organic components overlap significantly (Fig. 1d). Hence, in the following, we are investigating the combined carrier dynamics of PbI* and DBCz* in $DBCzPbI_3$. Consistent with the 0.65 eV blueshift of the excitonic peak in the absorption spectrum as compared to the 2D HOIP, the GSB of $DBCzPbI_3$ appears at 390 nm, again sandwiched between two typical PIA features (Fig. 4a and 4b). The PbI GSB obscures the DBCz GSB, but a noticeable spectral evolution indicates two overlapping features in the 380–400nm region. A similar broad PIA in the VIS spectral region (500–850 nm) is observed as in $(DBCz)_2PbI_4$ (Fig. 3b), again revealing the formation of $DBCz^{+\cdot}$. While in the spectra of the 2D HOIP, the perovskite PIA partially overlaps with the $DBCz^{+\cdot}$ PIA, the full DBCz-related PIA is clearly

resolved for $DBCzPbI_3$ (Fig. 4b), demonstrating an even closer resemblance to the propyl-DBCz hole polaron observed in solution (overlaid in Fig. 4b).

Although the appearance of such a sharp PIA peak at 550 nm in the early-time spectra could have been present for the 2D HOIP as well, obscured by the other spectral features, it might also indicate the formation of a more localized $DBCz^{+\cdot}$ hole polaron for the edge-sharing phase, which would agree with the more isolated DBCz molecules in $DBCzPbI_3$ compared to what is expected for the organic cation inside of a typical bilayer in a 2D HOIP such as $(DBCz)_2PbI_4$ (Fig. 1c). The pronounced localization of the hole on the 5-position (Fig. 1a) agrees with the large orbital density coefficients of the HOMO bands at this position (Fig. 2). We again rule out DBCz singlet related PIA features, as the DBCzI spectra are markedly different. Hence, both PbI* to DBCz hole transfer and DBCz* to PbI electron transfer are on an ultrafast (<200 fs) timescale.

The decay behavior of the ultrafast generated $DBCz^{+\cdot}$ species in $DBCzPbI_3$ is considerably different from that in $(DBCz)_2PbI_4$. From the UV TA maps in Fig. 4a and kinetics in Fig. 4c, a ~1–2 ns growth of a sharp 410 nm PIA can be seen. Although this feature overlaps with the typical perovskite PIA feature that appears next to the GSB signal at 390 nm, this growth does not represent a repopulation of carriers in the PbI states, as this would be associated with a rise in the GSB as well. Instead, we attribute this growth at 410 nm to a charge-transfer mediated formation of triplet states in DBCz.[59-62] Importantly, the 410 nm PIA agrees with the T_1 PIA previously observed for carbazole.[63] For DBCzI, no comparable growth of such a feature is observed (Fig. S18), consistent with the excited DBCz* species decaying predominantly via fluorescence rather than phosphorescence (Fig. 1d). This difference confirms that triplet formation proceeds via charge-transfer-mediated processes involving the inorganic framework. Nevertheless, the presence of a weak red shoulder in DBCzI suggests that a minor population decays via phosphorescence (Fig. 1d). This is confirmed by time-resolved PL measurements, which reveal a weak broad red-emitting species (500–700 nm) with a slower decay than the singlet fluorescence at 440 nm (Fig. S19). The spectral overlap with the reported phosphorescence spectrum of a DBCz isomer[64] supports its assignment to phosphorescence, although our measured spectrum is considerably broadened compared to the literature spectrum, which was recorded at cryogenic temperatures.

Consistent with the observation of triplets in $DBCzPbI_3$ from TA spectroscopy, the PL spectrum of $DBCzPbI_3$ also shows the phosphorescence band observed in DBCzI (Fig. 1d), indicating that a fraction of the triplet population decays radiatively. However, the strongly redshifted emission suggests the contribution of triplet excimer formation. This assignment is supported by the observed PL decay on a ~50 ns timescale—significantly longer than the typical radiative lifetimes of Wannier excitons in 2D perovskites—and by its acceleration under oxygen-rich conditions, consistent with triplet quenching (Fig. S20). Notably, this decay is much shorter than the reported triplet lifetimes of isolated carbazole[63] and a dibenzocarbazole derivative.[64] Similarly short triplet lifetimes have been observed for other chromophores embedded in perovskite lattices,[20, 59, 65] which may arise from the strong spin–orbit coupling of Pb and I atoms. In addition, the specific molecular stacking within the layered structure may facilitate triplet excimer formation.[20, 66] Note that under cryogenic conditions,[17, 67] the triplet lifetimes within the perovskite lattice may be significantly longer.

On the same timescale as the 410 nm PIA rise, a broad positive $\Delta T/T$ feature appears between 550–700 nm (Fig. 4b), which becomes more evident at higher excitation fluence (Fig. S21). This feature spectrally overlaps with the phosphorescence band observed in steady-state and time-resolved PL and can therefore be assigned to triplet-related stimulated emission. The broad featureless shape could indicate bleaching from defect states, although no ground-state absorption is observed in this spectral region (Fig. 1d). Additional photothermal deflection spectroscopy measurements confirm that ground-

state absorption does not occur within the relevant wavelength range. (Fig. S22). Instead, the broadening may arise from the chemical broadening associated with triplet excimer formation. The calculated distance between two DBCz molecules is ±3.6 Å, which is remarkably similar to the intermolecular distance of the organic molecules in a pyrene-based 2D HOIP in which the same phenomenon has been observed.[20] Similarly, the observed PL is more consistent with triplet emission rather than defect-related emission, as evidenced by its accelerated decay under oxygen-rich conditions. The sharper lineshape of triplet PIA compared to the emission can be attributed to overlapping bleach contributions from both DBCz and the PbI framework, and potentially also to differences in vibronic broadening between the $T_1 \rightarrow T_n$ and $T_1 \rightarrow S_0$ transitions.

Finally, a more pronounced fluence dependence (Fig. S23) in the decay curves of $DBCzPbI_3$ compared to $(DBCz)_2PbI_4$ indicates a charge separated state as the intermediate state for $DBCzPbI_3$ rather than a bound charge transfer state. This is consistent with the non-exponential rise kinetics of the 410 nm PIA (Fig. 4c). Alternatively, this fluence dependence could be an indication for triplet-triplet annihilation.[68]

In addition to the fluence dependence, the close match between the PIA band of $DBCzPbI_3$ and the oxidized DBCz spectrum supports the assignment to a hole polaron localized on DBCz. By contrast, the distinct photoinduced absorption spectrum observed in $(DBCz)_2PbI_4$ suggests that the electron–hole pair formed after charge transfer is weakly bound, leading to a slight perturbation of the DBCz transitions (although we note that additional factors could also contribute, *vide supra*).

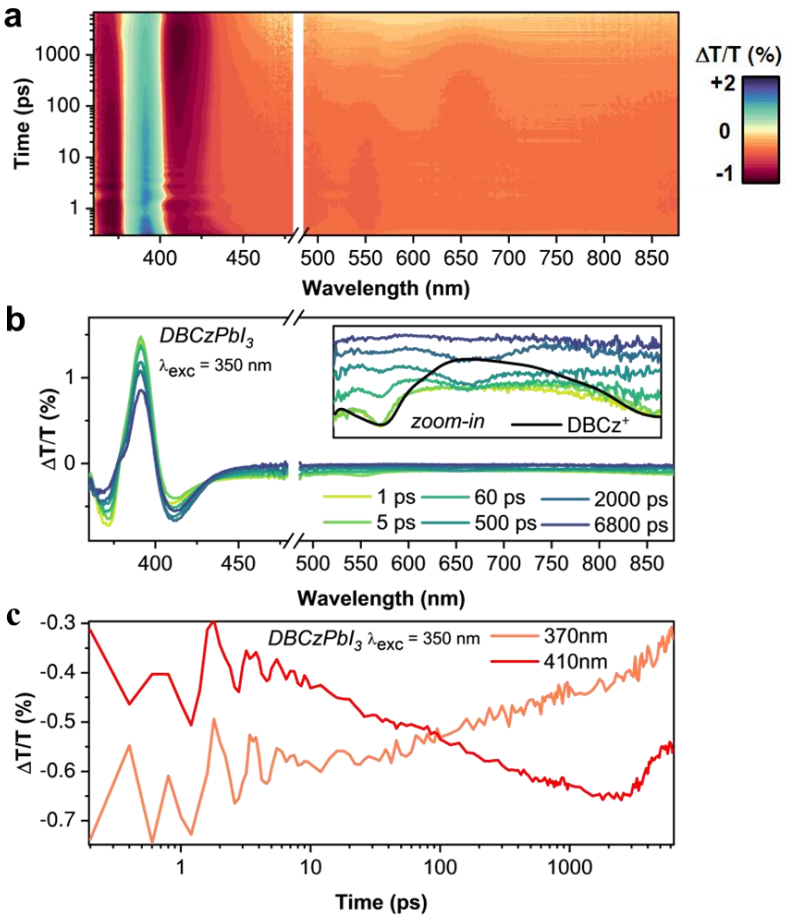

Figure 4. (a) Stitched UV and VIS transient absorption (TA) maps of a $DBCzPbI_3$ thin film photoexcited at 350 nm. A small spectral gap around 480—485 nm appears where the noise floor for both probes is relatively high. (b) Stitched UV and VIS TA spectra. The inset shows the zoomed-in VIS spectra (500–880 nm). The DBCz hole polaron spectrum, measured in solution (Fig. S13), is overlaid in black. (c) Kinetics probed at 370 nm and 410 nm with photoexcitation at 350 nm.

We present a schematic summary of the excited-state dynamics for both $(DBCz)_2PbI_4$ and $DBCzPbI_3$ in Fig. 5. Whereas energy transfer of the PbI excitons to the singlet manifold of DBCz is energetically non-spontaneous (Table S3), there is a strong driving force for hole transfer to DBCz. Due to different relative energies of the photoinduced intermediate states in the 2D HOIP and the edge-sharing phases, charge-transfer-mediated DBCz triplet formation only occurs significantly in $DBCzPbI_3$.

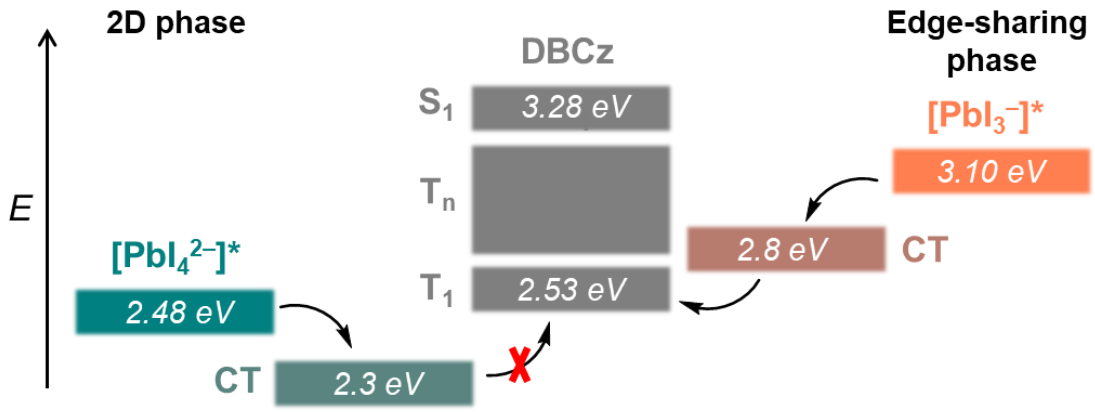

Fig. 5. Schematic state diagram and charge transfer (CT) dynamics in both $(DBCz)_2PbI_4$ and $DBCzPbI_3$. CT energy in $(DBCz)_2PbI_4$ is approximated from PbI* 1s - (VB,lit.[69] - HOMO-DBCz,CV) = 2.48 - (5.8-5.6) = 2.28 eV. CT energy in $DBCzPbI_3$ is approximated from the literature VBM value of 5.8 eV and CV-measured DBCz-HOMO of 5.6 eV for the 2D phase and from CBM,DFT - HOMO,DFT = 2.84 eV. Note that these CT energies do not account for_exciton delocalization, or dielectric screening, which may significantly alter the effective CT energy. The DBCz triplet values are also calculated from DFT (Table S3). PbI exciton energies are taken from experimental absorption spectra.

Coherent phonons in $DBCzPbI_3$

Picosecond oscillations, arising from impulsively excited coherent phonons, are visible in the UV-Vis transient absorption kinetics (Fig. 4c) and map (Fig. 4a) of $DBCzPbI_3$. For clarity, these features are replotted in Fig. 6a, showing the first 5 ps. To obtain the pure phonon coherences, the electronic decay component is first fitted and subtracted (Fig. 6b). Then, we apply a fast Fourier transformation (FFT) to obtain the corresponding resonant Raman spectrum, revealing an intense signal at 19 cm^{-1} (Fig. 6c). Faster oscillations with periods <400 fs are observed in the first ps in the 365–375 nm and 410–420 nm spectral regions, which cannot be accurately quantified in the present experiment (see SI Methods).

The spectral dependence of the 19 cm^{-1} mode FFT amplitude reveals two maxima, sandwiching a node centred at ~385 nm (Fig. 6d), 14 nm (0.11 eV) bluer than the excitonic resonance maximum of $DBCzPbI_3$. Generally, coherently excited phonons modulate the excitonic transitions *via* the Franck–Condon principle involving the displacement of the excited-state surface with respect to the ground-state surface (i.e. Huang–Rhys factor), characterized by a node at the centre of the absorption maximum of that coupled exciton.[70-72] In contrast, we observe a maximum FFT amplitude at the excitonic resonance, while the node appears closer to the second excitonic transition at 381 nm, corresponding to the first excited state of the DBCz molecule. This observation could lead one to suspect that the 19 cm^{-1} mode is an organic mode coupled to the organic exciton. However, it is unlikely that the edge-sharing PbI_3^- environment alone is the reason that organic phonon coherences appear in $DBCzPbI_3$ but are completely absent for DBCzI and $(DBCz)_2PbI_4$ (Fig. S24). Furthermore, the rest of the FFT profile is not consistent with such an assignment (Fig. S25). In particular, the strong amplitude at 400 nm—far from the organic exciton—can not be explained with a Franck-Condon modulated organic phonon. Even though a stimulated emission signal appears at 400 nm, the expected similar oscillator strength to the bleach transition can not account for the observed asymmetric FFT profile.

Instead, we assign the 19 cm^{-1} mode to a PbI_3^- phonon which modulates the PbI_3^- excitonic resonance *via* Herzberg-Teller coupling. Such a ''non-Condon'' coupling can brighten symmetry-forbidden transitions and results in *amplitude* rather than *frequency* modulation of the excitonic transitions.[73-77]

As the transition dipole moment is linearly dependent on the phonon coordinate, the spectral dependence of the FFT amplitude should coincide with the absorption spectrum. However, because the absorption spectrum of $DBCzPbI_3$ consists of both inorganic and organic transitions, and the PbI_3^- phonon is expected to couple most strongly to the inorganic transitions, we also plotted the FFT profile with the difference absorption spectra between $DBCzPbI_3$ and DBCzI to obtain an artificial inorganic absorption spectrum (Fig. S25). Consistent with a Herzberg–Teller coupled PbI_3^- mode, the phonon oscillations are in-phase across the absorption spectrum (Fig. 6b), resulting in a non-zero FFT value for the averaged phonon coherences (Fig. 6c).

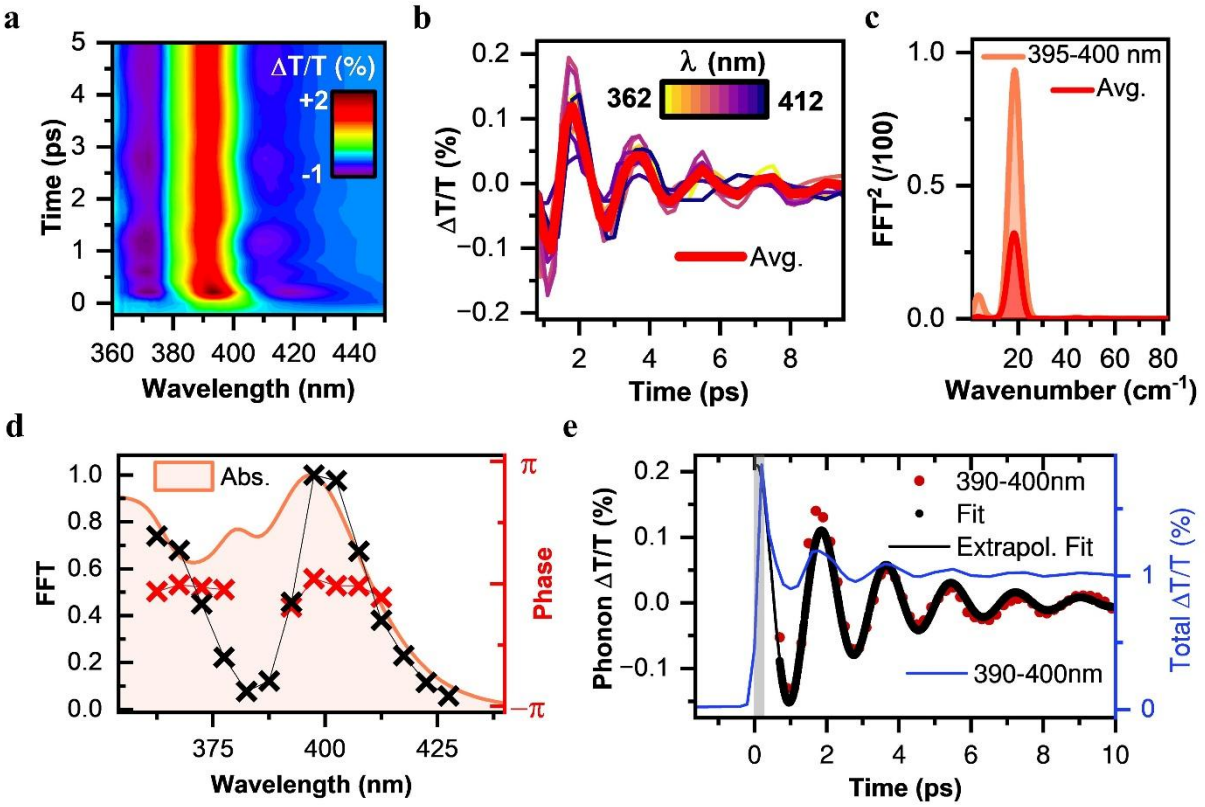

Fig. 6. (a) UV TA map of a $DBCzPbI_3$ thin film photoexcited at 350 nm, zoomed in at the first 5 ps. (b) Electronic-decay free pure phonon coherences of transients between 360 and 415 nm integrated in steps of 5 nm. The traces between 380 and 390 nm are excluded from the plot as well as the fitting. The averaged kinetic trace is shown in red. (c) Fast Fourier transform (FFT) of 395-400nm and averaged traces. FFT peaks are obtained at 19 cm^{-1} and 3 cm^{-1}. Note that the latter is an artefact from the FFT, as it corresponds to a period of 11 ps, well beyond the integrated time window. (d) Spectrally-dependent FFT amplitude and extrapolated phase, plotted together with the absorption spectrum. A 0.5π phase was added to extrapolated phases from fitting equation 1, such that they are in cosine form. (e) Phonon coherence transient and fit with parameters A=0.22, τ =2.8 ps, $\tilde{\nu}$=19 cm^{-1}, ϕ =0.4 π. The extrapolation to t_0 reveals that the oscillation is well described by a damped cosine. The "total" kinetic trace of 390-400 nm is plotted as well in blue to show the t_0 region (indicated with the grey box).

To quantify the phase of the phonon coherences, we fit the oscillatory traces to an exponentially damped sinusoid function (390-400 nm trace is shown as an example in Fig. 6e), representing a single harmonic oscillator with frequency ω, amplitude A that decays with a decoherence time τ through

various scattering mechanisms, including phonon-phonon, defect-phonon scattering and carrier-phonon:

$$g(t) = Ae^{-t/\tau}\sin(2\pi \cdot \omega t + \phi) \qquad \mathbf{1}$$

From this fit, we obtain a decoherence time of 2.8 ps and a frequency of 19 cm^{-1}, consistent with the above FFT analysis. Upon extrapolation of the fitted transient to t = 0 ps we find that it follows a cosine function, rather than a sine function (black line in Fig. 6e). The constant spectral phase across the PbI_3^- excitonic resonance supports the Herzberg-Teller coupling mechanism (Fig. 6d). In contrast, frequency modulated excited-state phonon wavepackets are typically associated with a π-phase jump around the excitonic resonance, in addition to the node.[70-72] Even though frequency modulated ground-state phonon wavepackets also do not show this π-phase jump, these should show a symmetric amplitude profile, whereas we observe a strongly asymmetric amplitude profile.

In addition to the *type* of phonon coherence modulation, the phase analysis may elucidate the *generation* mechanism of coherence. Based on the cosine functional form, we can conclude that the coherent phonon was either excited *via* the displacive excitation of coherent phonons (DECP) mechanism or through the resonant impulsive stimulated Raman scattering (RISRS) mechanism, whereas the off-resonant ISRS mechanism can be excluded.[78] We propose that the observed phonon wavepackets are generated via RISRS rather than DECP, as Herzberg–Teller coupling does not rely on a displaced excited state surface. Finally, the ultrafast charge transfer process itself may induce coherent phonons, provided that the rate of charge transfer is faster than the period of the phonon.[71, 79] In that case, there should be a deviation from the cosine function depending on the timescale of charge transfer, which we can not accurately determine with the limited time resolution of our experiment. The charge transfer and accompanying lattice relaxation may underlie the atypical ~ps-timescale blueshift—rather than the more common redshift—observed in the TA spectrum (Fig. 6a).

To further explore the aforementioned phonon mode revealed by UV TA kinetics, we performed DFT-based lattice dynamics simulations of $DBCzPbI_3$ (Fig. S26 and S27). From our calculations, we identify three Raman-active modes within 1 cm^{-1} of the experimentally observed 19 cm^{-1} mode (Fig. 6c). Of these, two modes exhibit B_{1g} symmetry, while the third exhibits fully symmetric A_g symmetry. We deconvolve these modes into contributions from the organic and inorganic components to investigate potential coupling pathways to electronic excitations (Fig. S26). We find that the B_{1g} mode (mode 21) with vibrational transition frequency 18.9 cm^{-1} is almost entirely composed of atomic displacement of the organic cation, and involves negligible motion of the inorganic framework. Consistently, the computed single particle energy difference for the optically allowed VBM→CBM+1 transition does not depend on this B_{1g} coordinate, as calculated with the displaced harmonic oscillators model (Fig. S28). Hence, this mode is unlikely to be the source of the observed oscillations. On the other hand, the more inorganic B_{1g} and A_{1g} modes (23 and 19, respectively) cause a stronger variation in the band gap. However, as the observed phonon coherence is of Herzberg-Teller type, Raman inactive modes should be considered as well (Fig. S26 and S27). Again, the nearly pure organic phonon mode (mode 22) can be excluded. In the case that the coherent phonon generation is charge-transfer induced (*vide supra*), the hybrid organic-inorganic B_{3u} mode is expected to be particularly active, as its vibrational motion aligns with the charge transfer coordinate. Lastly, we note that the phonon calculations described here were performed on the experimentally determined crystal structure, which includes a disordered alkyl chain. Due to this disorder, the vibrational analysis revealed imaginary modes entirely localized on these alkyl chains. As these imaginary vibrational modes involve no motions other than those of the alkyl chains, these imaginary modes are attributed to the intrinsic structural disorder of these groups, rather than inaccuracies or limitations of the employed theoretical method.

Considering that in most perovskite compositions—3D,[80-86] 2D,[72, 87-90] and nanocrystals[91, 92]—coherent phonons are severely damped at room temperature owing to the strong anharmonicity and dynamic disorder, the observed strong amplitude in $DBCzPbI_3$—up to 50% of the $\Delta T/T$ signal—is remarkable. In fact, phonon coherences in 2D HOIPs are typically only observed under cryogenic conditions to sufficiently reduce the phonon-phonon scattering component of the decoherence.[72, 87-90] Nonetheless, evident room temperature phonon coherences have been observed in Dion-Jacobson 2D perovskites,[93] bismuth-based 1D perovskites[94] and 2D lead-based hybrid chalcogenides,[95] likely related to enhanced lattice stiffness and more rigid bonding compared to the typical HOIPs. Although the prominent phonon coherences in $DBCzPbI_3$, but fully damped coherences in $(DBCz)_2PbI_4$, may be ascribed to reduced anharmonicity and therefore longer phonon decoherence times for the edge-sharing phase, the large amplitude must be related to strong exciton-phonon coupling. In previous reports on 3D and 2D perovskites, the observed phonon coherences are usually linked to charge–polaron[81, 83] and exciton–polaron[72, 89] formation, respectively. Due to large carrier delocalization in these systems, the coupling to phonons is generally weak, resulting in large—rather than small—polaron formation. Perovskites with a lower structural or electronic dimensionality than 2D, on the other hand, exhibit larger exciton-phonon coupling, which explains the ubiquitous observation of octahedral-distortion induced self-trapped exciton emission in these materials.[94, 96, 97] Indeed, particularly large phonon amplitudes have been reported in double perovskites,[98] where strong exciton–phonon coupling drives self-trapped exciton formation. Furthermore, distortions of the inorganic framework induced by the choice of organic spacer in Dion–Jacobson perovskites have been shown to enhance exciton–phonon coupling, manifesting as large coherent phonon amplitudes.[93] Consequently, we attribute the large amplitude of the coherent phonon mode in $DBCzPbI_3$ to its distorted edge-sharing PbI_6 octahedra (Fig. 1b), resulting in exciton localization and therefore strong exciton–phonon coupling. This coupling may be further enhanced by ultrafast charge transfer, which induces relaxation of the inorganic framework in response to changes in the exciton wavefunction. Further in-depth investigation of exciton–phonon coupling in $DBCzPbI_3$ is outside the scope of this communication and can be the subject of future work.

Conclusions

In this study, we show that *via* incorporation of the electroactive organic spacer, dibenzocarbazole (DBCz), two distinct low-dimensional hybrid metal halides can be obtained as thin films: a regular 2D HOIP ($(DBCz)_2PbI_4$) and a perovskite analogue with a 2D lead iodide framework ($DBCzPbI_3$). The crystal structure resolution of $DBCzPbI_3$ uncovers a layered metal halide framework with an edge-sharing octahedral motif, which has not been reported in the literature up until now. We found that by adjusting the stoichiometry of the precursor solution and by using a mixed thermal/solvent vapor annealing approach, phase-pure films of both phases could be obtained.

TA spectroscopy and DFT calculations have revealed how the octahedral connectivity controls the electronic structure and optical properties of these materials. Although the energy level alignment enables ultrafast photoinduced hole transfer from the inorganic to the organic layer in both phases, only in the edge-sharing phase is this charge transfer step followed by triplet formation, which is energetically not allowed for the 2D HOIP. In addition, the distorted edge-sharing octahedral framework in $DBCzPbI_3$ promotes strong Herzberg–Teller type exciton–phonon coupling, enabling coherent lattice vibrations at room temperature.

Author information

*Corresponding Authors:

Wouter T. M. Van Gompel

E-mail: wouter.vangompel@uhasselt.be

Samuel D. Stranks

E-mail: sds65@cam.ac.uk

Author Contributions

†These authors contributed equally to this work.

CRediT: I. D. (conceptualization, investigation, writing – original draft, writing – review & editing, visualization), Y. B. (conceptualization, investigation, writing – original draft, writing – review & editing, visualization, methodology), P. B. (investigation, methodology, visualization, writing – review & editing), Q. C. (investigation, methodology, writing – review & editing, supervision, funding acquisition), P. L. M. (investigation), A. C. (investigation), L. L. (funding acquisition, resources), E. D. (investigation, methodology), P. A. (supervision, funding acquisition), K. V. H. (supervision, funding acquisition, visualization, resources), D. B. (supervision, funding acquisition, resources, writing – review & editing), S. D. S. (supervision, funding acquisition, resources), W. T. M. V. G. (conceptualization, writing – original draft, writing – review & editing, supervision, funding acquisition, project administration).

The manuscript was written through the contributions of all authors. All authors have given approval to the final version of the manuscript.

Data availability statement

The data that support the findings of this study is available to download at the University of Cambridge's Apollo Repository [DOI to be added at acceptance].

Crystallographic data for $DBCzPbI_3$ has been deposited at the CCDC under 2471229.

Notes

The authors declare no competing financial interest.

Acknowledgements

I. D. and A. C. acknowledge the Research Foundation – Flanders (FWO) for the funding of their FWO strategic basic research PhD grants (1S31325N and 1SH0X24N, respectively). P. B., P. L. M., L. L., K. V. H., C. Q., D. B., and W. T. M. V. G. acknowledge the FWO for funding through the FWO research project G0A8723N. C. Q., D. B., and W. T. M. V. G. acknowledge the FWO (G0AQV25N) and the FNRS (n° T.0009.25) for funding through the WEAVE research project INTENSITY. This work was supported by Hasselt University and the FWO via the Hercules projects AUHL/15/2-GOH3816N and I001324N. C. Q. is a FNRS Research Associate and D. B. is FNRS Research Director. Y. B. acknowledges the Winton Programme for Physics of Sustainability for funding. S. D. S. acknowledges the Royal Society and Tata Group (grant numbers UF150033, URF\R\221026). Huguette Penxten and dr. Sander Smeets (UHasselt) are acknowledged and thanked for their help with the CV and NMR measurements, respectively. Prof. dr. Akshay Rao (University of Cambridge, UK) and Prof. dr. Daniel B. Turner (Boise State University, US) are thanked for fruitful discussions related to the coherent phonons in $DBCzPbI_3$.

References

(1) Li, W.; Li, M.; He, Y.; Song, J.; Guo, K.; Pan, W.; Wei, H. Arising 2D Perovskites for Ionizing Radiation Detection. *Adv Mater* **2024**, *36* (26), e2309588. DOI: 10.1002/adma.202309588 From NLM PubMed-not-MEDLINE.

(2) Jung, E. I.; Lee, H. J.; Kim, J.; Siddiqui, Q. T.; Kim, M.; Lin, Z.; Park, C.; Ha Kim, D. Recent progress on chiral perovskites as chiroptical active layers for next-generation LEDs. *Mat Sci Eng R* **2024**, *160*, 100817. DOI: ARTN 100817

10.1016/j.mser.2024.100817.

(3) Duan, J.; Li, J.; Divitini, G.; Cortecchia, D.; Yuan, F.; You, J.; Liu, S. F.; Petrozza, A.; Wu, Z.; Xi, J. 2D Hybrid Perovskites: From Static and Dynamic Structures to Potential Applications. *Adv Mater* **2024**, *36* (30), e2403455. DOI: 10.1002/adma.202403455 From NLM PubMed-not-MEDLINE.

(4) Liu, S. W.; Biju, V. P.; Qi, Y. B.; Chen, W.; Liu, Z. H. Recent progress in the development of high-efficiency inverted perovskite solar cells. *Npg Asia Mater* **2023**, *15* (1), 27. DOI: ARTN 27

10.1038/s41427-023-00474-z.

(5) Li, X.; Hoffman, J. M.; Kanatzidis, M. G. The 2D Halide Perovskite Rulebook: How the Spacer Influences Everything from the Structure to Optoelectronic Device Efficiency. *Chem Rev* **2021**, *121* (4), 2230–2291. DOI: 10.1021/acs.chemrev.0c01006 From NLM PubMed-not-MEDLINE.

(6) Boeije, Y.; Van Gompel, W. T. M.; Zhang, Y.; Ghosh, P.; Zelewski, S. J.; Maufort, A.; Roose, B.; Ooi, Z. Y.; Chowdhury, R.; Devroey, I.; et al. Tailoring Interlayer Charge Transfer Dynamics in 2D Perovskites with Electroactive Spacer Molecules. *J Am Chem Soc* **2023**, *145* (39), 21330–21343. DOI: 10.1021/jacs.3c05974 From NLM PubMed-not-MEDLINE.

(7) Van Gompel, W. T. M.; Lutsen, L.; Vanderzande, D. 2D and quasi-2D hybrid perovskites containing organic cations with an extended conjugated system: opportunities and challenges. *Journal of Materials Chemistry C* **2023**, *11* (38), 12877–12893. DOI: 10.1039/d3tc02553e.

(8) Sun, J.; Wang, K.; Ma, K.; Park, J. Y.; Lin, Z. Y.; Savoie, B. M.; Dou, L. Emerging Two-Dimensional Organic Semiconductor-Incorporated Perovskites horizontal line A Fascinating Family of Hybrid Electronic Materials. *J Am Chem Soc* **2023**, *145* (38), 20694–20715. DOI: 10.1021/jacs.3c02143 From NLM Publisher.

(9) Yang, J.; He, T. W.; Li, M.; Li, G. X.; Liu, H. R.; Xu, J. J.; Zhang, M.; Zuo, W. W.; Qin, R. P.; Aldamasy, M. H.; et al. π-Conjugated Carbazole Cations Enable Wet-Stable Quasi-2D Perovskite Photovoltaics. *Acs Energy Letters* **2022**, *7* (12), 4451–4458. DOI: 10.1021/acsenergylett.2c02219.

(10) Herckens, R.; Van Gompel, W. T. M.; Song, W.; Gélvez-Rueda, M. C.; Maufort, A.; Ruttens, B.; D'Haen, J.; Grozema, F. C.; Aernouts, T.; Lutsen, L.; et al. Multi-layered hybrid perovskites templated with carbazole derivatives: optical properties, enhanced moisture stability and solar cell characteristics. *Journal of Materials Chemistry A* **2018**, *6* (45), 22899–22908, 10.1039/C8TA08019D. DOI: 10.1039/C8TA08019D.

(11) Van Landeghem, M.; Van Gompel, W.; Herckens, R.; Lutsen, L.; Vanderzande, D.; Van Doorslaer, S.; Goovaerts, E. Light-Induced Charge Transfer in Two-Dimensional Hybrid Lead Halide Perovskites. *The Journal of Physical Chemistry C* **2021**, *125* (33), 18317–18327. DOI: 10.1021/acs.jpcc.1c05005.

(12) Era, M.; Yasuda, T.; Mori, K.; Tomotsu, N.; Kawano, N.; Koshimizu, M.; Asai, K. PbBr-Based Layered Perovskite Organic-Inorganic Superlattice Having Carbazole Chromophore; Hole-Mobility and Quantum Mechanical Calculation. *J Nanosci Nanotechnol* **2016**, *16* (4), 3159–3167. DOI: 10.1166/jnn.2016.12320 From NLM PubMed-not-MEDLINE.

(13) Jeong, J.; Chawanpunyawat, T.; Kim, M.; Sláma, V.; Lempesis, N.; Agosta, L.; Carnevali, V.; Zhang, Q. H.; Eickemeyer, F. T.; Pfeifer, L.; et al. Carbazole Treated Waterproof Perovskite Films with Improved Solar Cell Performance. *Adv Energy Mater* **2025**, *15* (2). DOI: 10.1002/aenm.202401965.

(14) Alphenaar, A. N.; Zhang, X. Y.; Xu, Y. Z.; Ramakrishnan, S.; Zhang, Y. G.; Yu, Q. M. Self-powered photodetectors based on Ruddlesden-Popper 2D hybrid perovskites with carbazole derivatives. *Appl Phys Lett* **2023**, *123* (25). DOI: Artn 251113

10.1063/5.0179297.

(15) Passarelli, J. V.; Fairfield, D. J.; Sather, N. A.; Hendricks, M. P.; Sai, H.; Stern, C. L.; Stupp, S. I. Enhanced Out-of-Plane Conductivity and Photovoltaic Performance in n = 1 Layered Perovskites through Organic Cation Design. *J Am Chem Soc* **2018**, *140* (23), 7313–7323. DOI: 10.1021/jacs.8b03659 From NLM PubMed-not-MEDLINE.

(16) Xue, J.; Wang, R.; Chen, X.; Yao, C.; Jin, X.; Wang, K. L.; Huang, W.; Huang, T.; Zhao, Y.; Zhai, Y.; et al. Reconfiguring the band-edge states of photovoltaic perovskites by conjugated organic cations. *Science* **2021**, *371* (6529), 636–640. DOI: 10.1126/science.abd4860 From NLM PubMed-not-MEDLINE.

(17) Braun, M.; Tuffentsammer, W.; Wachtel, H.; Wolf, H. C. Pyrene as emitting chromophore in organic-inorganic lead halide-based layered perovskites with different halides. *Chem Phys Lett* **1999**, *307* (5-6), 373–378. DOI: Doi 10.1016/S0009-2614(99)00526-6.

(18) Marchal, N.; Van Gompel, W.; Gélvez-Rueda, M. C.; Vandewal, K.; Van Hecke, K.; Boyen, H. G.; Conings, B.; Herckens, R.; Maheshwar, S.; Lutsen, L.; et al. Lead-Halide Perovskites Meet Donor-Acceptor Charge-Transfer Complexes. *Chemistry of Materials* **2019**, *31* (17), 6880–6888. DOI: 10.1021/acs.chemmater.9b01289.

(19) Hooijer, R.; Wang, S.; Biewald, A.; Eckel, C.; Righetto, M.; Chen, M.; Xu, Z.; Blatte, D.; Han, D.; Ebert, H.; et al. Overcoming Intrinsic Quantum Confinement and Ultrafast Self-Trapping in Ag-Bi-I- and Cu-Bi-I-Based 2D Double Perovskites through Electroactive Cations. *J Am Chem Soc* **2024**, *146* (39), 26694–26706. DOI: 10.1021/jacs.4c04616 From NLM PubMed-not-MEDLINE.

(20) De, A.; Mora Perez, C.; Liang, A.; Wang, K.; Dou, L.; Prezhdo, O.; Huang, L. Tunneling-Driven Marcus-Inverted Triplet Energy Transfer in a Two-Dimensional Perovskite. *J Am Chem Soc* **2024**, *146* (6), 4260–4269. DOI: 10.1021/jacs.4c00236 From NLM PubMed-not-MEDLINE.

(21) Ni, X. J.; Li, H.; Brédas, J. L. Enhanced Organic-Inorganic Electronic Coupling in Two-Dimensional Hybrid Perovskites through Molecular Engineering of Dipolar Pyrene-Based Cations. *Acs Materials Letters* **2024**, *6* (8), 3436–3442. DOI: 10.1021/acsmaterialslett.4c00995.

(22) Gao, Y.; Shi, E.; Deng, S.; Shiring, S. B.; Snaider, J. M.; Liang, C.; Yuan, B.; Song, R.; Janke, S. M.; Liebman-Pelaez, A.; et al. Molecular engineering of organic-inorganic hybrid perovskites quantum wells. *Nat Chem* **2019**, *11* (12), 1151–1157. DOI: 10.1038/s41557-019-0354-2 From NLM PubMed-not-MEDLINE.

(23) Mitzi, D. B.; Chondroudis, K.; Kagan, C. R. Design, Structure, and Optical Properties of Organic-Inorganic Perovskites Containing an Oligothiophene Chromophore. *Inorg Chem* **1999**, *38* (26), 6246–6256. DOI: 10.1021/ic991048k From NLM PubMed-not-MEDLINE.

(24) Ou, Z.; Wang, C.; Tao, Z. G.; Li, Y.; Li, Z.; Zeng, Y.; Li, Y.; Shi, E.; Chu, W.; Wang, T.; et al. Organic Ligand Engineering for Tailoring Electron-Phonon Coupling in 2D Hybrid Perovskites. *Nano Lett* **2024**, *24* (20), 5975–5983. DOI: 10.1021/acs.nanolett.4c00463 From NLM PubMed-not-MEDLINE.

(25) Dong, X.; Wang, R.; Gao, Y.; Ling, Q.; Hu, Z.; Chen, M.; Liu, H.; Liu, Y. Orbital Interactions in 2D Dion-Jacobson Perovskites Using Oligothiophene-Based Semiconductor Spacers Enable Efficient Solar Cells. *Nano Lett* **2024**, *24* (1), 261–269. DOI: 10.1021/acs.nanolett.3c03887 From NLM PubMed-not-MEDLINE.

(26) Guo, S.; Li, Y.; Mao, Y.; Tao, W.; Bu, K.; Fu, T.; Zhao, C.; Luo, H.; Hu, Q.; Zhu, H.; et al. Reconfiguring band-edge states and charge distribution of organic semiconductor-incorporated 2D perovskites via pressure gating. *Sci Adv* **2022**, *8* (44), eadd1984. DOI: 10.1126/sciadv.add1984 From NLM PubMed-not-MEDLINE.

(27) Ledee, F.; Audebert, P.; Trippe-Allard, G.; Galmiche, L.; Garrot, D.; Marrot, J.; Lauret, J. S.; Deleporte, E.; Katan, C.; Even, J.; et al. Tetrazine molecules as an efficient electronic diversion channel in 2D organic-inorganic perovskites. *Mater Horiz* **2021**, *8* (5), 1547–1560. DOI: 10.1039/d0mh01904f From NLM PubMed-not-MEDLINE.

(28) Nussbaum, S.; Socie, E.; Fish, G. C.; Diercks, N. J.; Hempel, H.; Friedrich, D.; Moser, J. E.; Yum, J. H.; Sivula, K. Photogenerated charge transfer in Dion-Jacobson type layered perovskite based on naphthalene diimide. *Chem Sci* **2023**, *14* (22), 6052–6058. DOI: 10.1039/d3sc00783a From NLM PubMed-not-MEDLINE.

(29) Nussbaum, S.; Tsokkou, D.; Frei, A. T.; Friedrich, D.; Moser, J. E.; Banerji, N.; Yum, J. H.; Sivula, K. Free Charge Carrier Generation by Visible-Light-Absorbing Organic Spacers in Ruddlesden-Popper Layered Perovskites. *J Am Chem Soc* **2024**, *146* (40), 27770–27778. DOI: 10.1021/jacs.4c09706 From NLM PubMed-not-MEDLINE.

(30) Nussbaum, S.; Socie, E.; Yao, L.; Yum, J.-H.; Moser, J.-E.; Sivula, K. Tuning Napththalenediimide Cations for Incorporation into Ruddlesden–Popper-Type Hybrid Perovskites. *Chemistry of Materials* **2022**, *34* (8), 3798–3805. DOI: 10.1021/acs.chemmater.2c00246.

(31) Feng, Z.; Liu, X.; Imaoka, K.; Ishii, T.; Tumen-Ulzii, G.; Tang, X.; Harrington, G. F.; Heinrich, B.; Ribierre, J. C.; Chamoreau, L. M.; et al. Artificial p–n-like Junction Based on Pure 2D Organic–Inorganic Halide Perovskite Structure Having Naphthalene Diimide Acceptor Moieties. *Advanced Optical Materials* **2023**, *11* (10), 2202734. DOI: 10.1002/adom.202202734.

(32) Duan, D. W.; Ge, C. Y.; Rahaman, M. Z.; Lin, C. H.; Shi, Y. M.; Lin, H. R.; Hu, H. L.; Wu, T. M. Recent progress with one-dimensional metal halide perovskites: from rational synthesis to optoelectronic applications. *Npg Asia Mater* **2023**, *15* (1), 8. DOI: ARTN 8

10.1038/s41427-023-00465-0.

(33) Mercier, N. Hybrid Halide Perovskites: Discussions on Terminology and Materials. *Angew Chem Int Ed Engl* **2019**, *58* (50), 17912–17917. DOI: 10.1002/anie.201909601 From NLM PubMed-not-MEDLINE.

(34) Shen, W. C.; Azmy, A.; Li, G.; Mishra, A.; Syrgiannis, Z.; Zheng, W. W.; Volonakis, G.; Kepenekian, M.; Even, J.; Wojtas, L.; et al. A Crystalline 2D Fullerene-Based Metal Halide Semiconductor for Efficient and Stable Ideal-bandgap Perovskite Solar Cells. *Adv Energy Mater* **2024**, *14* (23). DOI: 10.1002/aenm.202400582.

(35) Gilley, I. W.; Wiggins, T. E.; Sargent, E. H.; Kanatzidis, M. G. Perovskitoids as Functional Materials. *Accounts of Chemical Research* **2025**. DOI: 10.1021/acs.accounts.5c00240.

(36) Lédée, F.; Trippé-Allard, G.; Diab, H.; Audebert, P.; Garrot, D.; Lauret, J.-S.; Deleporte, E. Fast growth of monocrystalline thin films of 2D layered hybrid perovskite. *CrystEngComm* **2017**, *19* (19), 2598–2602. DOI: 10.1039/c7ce00240h.

(37) Denis, P.-H.; Mertens, M.; Van Gompel, W. T. M.; Van Hecke, K.; Ruttens, B.; D'Haen, J.; Lutsen, L.; Vanderzande, D. Directing the Self-Assembly of Conjugated Organic Ammonium Cations in Low-Dimensional Perovskites by Halide Substitution. *Chemistry of Materials* **2021**, *33* (13), 5177–5188. DOI: 10.1021/acs.chemmater.1c01221.

(38) Van Gompel, W. T. M.; Herckens, R.; Van Hecke, K.; Ruttens, B.; D'Haen, J.; Lutsen, L.; Vanderzande, D. Low-Dimensional Hybrid Perovskites Containing an Organic Cation with an Extended Conjugated System: Tuning the Excitonic Absorption Features. *Chemnanomat* **2019**, *5* (3), 323–327. DOI: 10.1002/cnma.201800561.

(39) Jana, M. K.; Song, R.; Xie, Y.; Zhao, R.; Sercel, P. C.; Blum, V.; Mitzi, D. B. Structural descriptor for enhanced spin-splitting in 2D hybrid perovskites. *Nat Commun* **2021**, *12* (1), 4982. DOI: 10.1038/s41467-021-25149-7 From NLM PubMed-not-MEDLINE.

(40) Kepenekian, M.; Traore, B.; Blancon, J. C.; Pedesseau, L.; Tsai, H.; Nie, W.; Stoumpos, C. C.; Kanatzidis, M. G.; Even, J.; Mohite, A. D.; et al. Concept of Lattice Mismatch and Emergence of Surface States in Two-dimensional Hybrid Perovskite Quantum Wells. *Nano Lett* **2018**, *18* (9), 5603–5609. DOI: 10.1021/acs.nanolett.8b02078 From NLM PubMed-not-MEDLINE.

(41) Liang, A. H.; Ma, K.; Gao, Y.; Dou, L. T. Tailoring Anchoring Groups in Low-Dimensional Organic Semiconductor-Incorporated Perovskites. *Small Struct* **2022**, *3* (3), 2100173. DOI: ARTN 2100173

10.1002/sstr.202100173.

(42) Xu, Z. T.; Mitzi, D. B. SnI-based hybrid perovskites templated by multiple organic cations:: Combining organic functionalities through noncovalent interactions. *Chemistry of Materials* **2003**, *15* (19), 3632–3637. DOI: 10.1021/cm034267j.

(43) Van Gompel, W. T. M.; Herckens, R.; Denis, P.-H.; Mertens, M.; Gélvez-Rueda, M. C.; Van Hecke, K.; Ruttens, B.; D'Haen, J.; Grozema, F. C.; Lutsen, L.; et al. 2D layered perovskite containing functionalised benzothieno-benzothiophene molecules: formation, degradation, optical properties and photoconductivity. *Journal of Materials Chemistry C* **2020**, *8* (21), 7181–7188. DOI: 10.1039/d0tc01053g.

(44) Du, K. Z.; Tu, Q.; Zhang, X.; Han, Q.; Liu, J.; Zauscher, S.; Mitzi, D. B. Two-Dimensional Lead(II) Halide-Based Hybrid Perovskites Templated by Acene Alkylamines: Crystal Structures, Optical Properties, and Piezoelectricity. *Inorg Chem* **2017**, *56* (15), 9291–9302. DOI: 10.1021/acs.inorgchem.7b01094 From NLM PubMed-not-MEDLINE.

(45) Kamminga, M. E.; de Wijs, G. A.; Havenith, R. W. A.; Blake, G. R.; Palstra, T. T. M. The Role of Connectivity on Electronic Properties of Lead Iodide Perovskite-Derived Compounds. *Inorg Chem* **2017**, *56* (14), 8408–8414. DOI: 10.1021/acs.inorgchem.7b01096 From NLM PubMed-not-MEDLINE.

(46) Karon, K.; Lapkowski, M. Carbazole electrochemistry: a short review. *Journal of Solid State Electrochemistry* **2015**, *19* (9), 2601–2610. DOI: 10.1007/s10008-015-2973-x.

(47) Peintinger, M. F.; Oliveira, D. V.; Bredow, T. Consistent Gaussian basis sets of triple-zeta valence with polarization quality for solid-state calculations. *Journal of Computational Chemistry* **2013**, *34* (6), 451–459. DOI: https://doi.org/10.1002/jcc.23153 (accessed 2025/09/29).

(48) Perdew, J. P.; Burke, K.; Ernzerhof, M. Generalized Gradient Approximation Made Simple. *Physical Review Letters* **1996**, *77* (18), 3865–3868. DOI: 10.1103/PhysRevLett.77.3865.

(49) Grimme, S.; Antony, J.; Ehrlich, S.; Krieg, H. A consistent and accurate ab initio parametrization of density functional dispersion correction (DFT-D) for the 94 elements H-Pu. *The Journal of Chemical Physics* **2010**, *132* (15), 154104. DOI: 10.1063/1.3382344 (accessed 6/15/2025).

(50) Pedesseau, L.; Sapori, D.; Traore, B.; Robles, R.; Fang, H. H.; Loi, M. A.; Tsai, H.; Nie, W.; Blancon, J. C.; Neukirch, A.; et al. Advances and Promises of Layered Halide Hybrid Perovskite Semiconductors. *ACS Nano* **2016**, *10* (11), 9776–9786. DOI: 10.1021/acsnano.6b05944 From NLM PubMed-not-MEDLINE.

(51) Garba, I. B.; Trombini, L.; Katan, C.; Even, J.; Zacharias, M.; Kepenekian, M.; Volonakis, G. Three-Dimensional to Layered Halide Perovskites: A Parameter-Free Hybrid Functional Method for Predicting Electronic Band Gaps. *ACS Materials Letters* **2025**, *7* (5), 1922–1929. DOI: 10.1021/acsmaterialslett.5c00158.

(52) Quarti, C.; Marchal, N.; Beljonne, D. Tuning the Optoelectronic Properties of Two-Dimensional Hybrid Perovskite Semiconductors with Alkyl Chain Spacers. *J Phys Chem Lett* **2018**, *9* (12), 3416–3424. DOI: 10.1021/acs.jpclett.8b01309 From NLM PubMed-not-MEDLINE.

(53) Blancon, J. C.; Stier, A. V.; Tsai, H.; Nie, W.; Stoumpos, C. C.; Traore, B.; Pedesseau, L.; Kepenekian, M.; Katsutani, F.; Noe, G. T.; et al. Scaling law for excitons in 2D perovskite quantum wells. *Nat Commun* **2018**, *9* (1), 2254. DOI: 10.1038/s41467-018-04659-x From NLM PubMed-not-MEDLINE.

(54) Manser, J. S.; Christians, J. A.; Kamat, P. V. Intriguing Optoelectronic Properties of Metal Halide Perovskites. *Chem Rev* **2016**, *116* (21), 12956–13008. DOI: 10.1021/acs.chemrev.6b00136 From NLM PubMed-not-MEDLINE.

(55) Price, M. B.; Butkus, J.; Jellicoe, T. C.; Sadhanala, A.; Briane, A.; Halpert, J. E.; Broch, K.; Hodgkiss, J. M.; Friend, R. H.; Deschler, F. Hot-carrier cooling and photoinduced refractive index changes in organic–inorganic lead halide perovskites. *Nature Communications* **2015**, *6* (1), 8420. DOI: 10.1038/ncomms9420.

(56) Fichou, D.; Horowitz, G.; Garnier, F. Polaron and bipolaron formation on isolated model thiophene oligomers in solution. *Synthetic Metals* **1990**, *39* (1), 125–131. DOI: https://doi.org/10.1016/0379-6779(90)90207-2.

(57) Gélvez-Rueda, M. C.; Van Gompel, W. T. M.; Herckens, R.; Lutsen, L.; Vanderzande, D.; Grozema, F. C. Inducing Charge Separation in Solid-State Two-Dimensional Hybrid Perovskites through the Incorporation of Organic Charge-Transfer Complexes. *The Journal of Physical Chemistry Letters* **2020**, *11* (3), 824–830. DOI: 10.1021/acs.jpclett.9b03746.

(58) Yang, Y.; Ostrowski, D. P.; France, R. M.; Zhu, K.; van de Lagemaat, J.; Luther, J. M.; Beard, M. C. Observation of a hot-phonon bottleneck in lead-iodide perovskites. *Nature Photonics* **2015**, *10* (1), 53–59. DOI: 10.1038/nphoton.2015.213.

(59) Lin, Y. L.; Johnson, J. C. Interlayer Triplet Energy Transfer in Dion–Jacobson Two-Dimensional Lead Halide Perovskites Containing Naphthalene Diammonium Cations. *The Journal of Physical Chemistry Letters* **2021**, *12* (20), 4793–4798. DOI: 10.1021/acs.jpclett.1c01232.

(60) Chakkamalayath, J.; Martin, L. E.; Kamat, P. V. Energy Cascade in Halide Perovskite-Multiple Chromophore Films: Direct versus Mediated Transfer. *ACS Photonics* **2024**, *11* (4), 1821–1831. DOI: 10.1021/acsphotonics.4c00354.

(61) Luo, X.; Liang, G.; Han, Y.; Li, Y.; Ding, T.; He, S.; Liu, X.; Wu, K. Triplet Energy Transfer from Perovskite Nanocrystals Mediated by Electron Transfer. *J Am Chem Soc* **2020**, *142* (25), 11270–11278. DOI: 10.1021/jacs.0c04583 From NLM PubMed-not-MEDLINE.

(62) Luo, X.; Han, Y.; Chen, Z.; Li, Y.; Liang, G.; Liu, X.; Ding, T.; Nie, C.; Wang, M.; Castellano, F. N.; et al. Mechanisms of triplet energy transfer across the inorganic nanocrystal/organic molecule interface. *Nature Communications* **2020**, *11* (1), 28. DOI: 10.1038/s41467-019-13951-3.

(63) Knötig, K. M.; Gust, D.; Lenzer, T.; Oum, K. Excited-State Dynamics of Carbazole and tert-Butyl-Carbazole in Organic Solvents. In *Photochem*, 2024; Vol. 4, pp 163–178.

(64) Zhang, X.; Chong, K. C.; Xie, Z.; Liu, B. Color-Tunable Dual-Mode Organic Afterglow for White-Light Emission and Information Encryption Based on Carbazole Doping. *Angewandte Chemie International Edition* **2023**, *62* (45), e202310335. DOI: https://doi.org/10.1002/anie.202310335 (accessed 2025/06/25).

(65) Tang, Y. H.; Yang, H. J.; Sun, J. A.; Wu, Z. J.; Shao, W. H.; Joy, S.; Kim, J. H.; Xu, W. Z.; Coffey, A. H.; Lee, Y. H.; et al. Triplet Management at Ligand-Perovskite Interface to Enhanced Photovoltaics Performance. *Acs Energy Letters* **2024**, *9* (9), 4323–4330. DOI: 10.1021/acsenergylett.4c01853.

(66) Tian, Y.; Li, Y.; Chen, B.; Lai, R.; He, S.; Luo, X.; Han, Y.; Wei, Y.; Wu, K. Sensitized Molecular Triplet and Triplet Excimer Emission in Two-Dimensional Hybrid Perovskites. *J Phys Chem Lett* **2020**, *11* (6), 2247–2255. DOI: 10.1021/acs.jpclett.0c00360 From NLM PubMed-not-MEDLINE.

(67) Ema, K.; Inomata, M.; Kato, Y.; Kunugita, H.; Era, M. Nearly perfect triplet-triplet energy transfer from Wannier excitons to naphthalene in organic-inorganic hybrid quantum-well materials. *Phys Rev Lett* **2008**, *100* (25), 257401. DOI: 10.1103/PhysRevLett.100.257401 From NLM PubMed-not-MEDLINE.

(68) Deng, Y.; Jiang, L.; Huang, L.; Zhu, T. Energy Flow in Hybrid Organic/Inorganic Systems for Triplet–Triplet Annihilation Upconversion. *ACS Energy Letters* **2022**, *7* (2), 847–861. DOI: 10.1021/acsenergylett.1c02648.

(69) Yin, J.; Bakr, O. M.; Mohammed, O. F. Intriguing Ultrafast Charge Carrier Dynamics in Two-Dimensional Ruddlesden-Popper Hybrid Perovskites. *J Phys Chem C* **2021**, *125* (18), 9630–9637. DOI: 10.1021/acs.jpcc.1c01944.

(70) Arpin, P. C.; Turner, D. B. Signatures of Vibrational and Electronic Quantum Beats in Femtosecond Coherence Spectra. *The Journal of Physical Chemistry A* **2021**, *125* (12), 2425–2435. DOI: 10.1021/acs.jpca.0c10807.

(71) Kumar, A. T. N.; Rosca, F.; Widom, A.; Champion, P. M. Investigations of amplitude and phase excitation profiles in femtosecond coherence spectroscopy. *The Journal of Chemical Physics* **2001**, *114* (2), 701–724. DOI: 10.1063/1.1329640 (accessed 6/14/2025).

(72) Thouin, F.; Valverde-Chavez, D. A.; Quarti, C.; Cortecchia, D.; Bargigia, I.; Beljonne, D.; Petrozza, A.; Silva, C.; Srimath Kandada, A. R. Phonon coherences reveal the polaronic character of excitons in two-dimensional lead halide perovskites. *Nat Mater* **2019**, *18* (4), 349–356. DOI: 10.1038/s41563-018-0262-7 From NLM PubMed-not-MEDLINE.

(73) Kano, H.; Saito, T.; Kobayashi, T. Observation of Herzberg−Teller-type Wave Packet Motion in Porphyrin J-Aggregates Studied by Sub-5-fs Spectroscopy. *The Journal of Physical Chemistry A* **2002**, *106* (14), 3445–3453. DOI: 10.1021/jp012493f.

(74) Son, D. H.; Kambhampati, P.; Kee, T. W.; Barbara, P. F. Femtosecond Multicolor Pump−Probe Study of Ultrafast Electron Transfer of [(NH3)5RuIIINCRuII(CN)5]- in Aqueous Solution. *The Journal of Physical Chemistry A* **2002**, *106* (18), 4591–4597. DOI: 10.1021/jp014151f.

(75) Ishii, K.; Takeuchi, S.; Tahara, T. Pronounced Non-Condon Effect as the Origin of the Quantum Beat Observed in the Time-Resolved Absorption Signal from Excited-State cis-Stilbene. *The Journal of Physical Chemistry A* **2008**, *112* (11), 2219–2227. DOI: 10.1021/jp077402e.

(76) Yoneda, Y.; Sotome, H.; Mathew, R.; Lakshmanna, Y. A.; Miyasaka, H. Non-condon Effect on Ultrafast Excited-State Intramolecular Proton Transfer. *The Journal of Physical Chemistry A* **2020**, *124* (2), 265–271. DOI: 10.1021/acs.jpca.9b09085.

(77) Kim, P.; Roy, S.; Valentine, A. J. S.; Liu, X.; Kromer, S.; Kim, T. W.; Li, X.; Castellano, F. N.; Chen, L. X. Real-time capture of nuclear motions influencing photoinduced electron transfer. *Chemical Science* **2024**, *15* (36), 14766–14777, 10.1039/D4SC01876A. DOI: 10.1039/D4SC01876A.

(78) Zeiger, H. J.; Vidal, J.; Cheng, T. K.; Ippen, E. P.; Dresselhaus, G.; Dresselhaus, M. S. Theory for displacive excitation of coherent phonons. *Phys Rev B* **1992**, *45* (2), 768–778. DOI: 10.1103/PhysRevB.45.768.

(79) Rather, S. R.; Fu, B.; Kudisch, B.; Scholes, G. D. Interplay of vibrational wavepackets during an ultrafast electron transfer reaction. *Nature Chemistry* **2021**, *13* (1), 70–77. DOI: 10.1038/s41557-020-00607-9.

(80) Ghosh, T.; Aharon, S.; Etgar, L.; Ruhman, S. Free Carrier Emergence and Onset of Electron–Phonon Coupling in Methylammonium Lead Halide Perovskite Films. *Journal of the American Chemical Society* **2017**, *139* (50), 18262–18270. DOI: 10.1021/jacs.7b09508.

(81) Duan, H.-G.; Tiwari, V.; Jha, A.; Berdiyorov, G. R.; Akimov, A.; Vendrell, O.; Nayak, P. K.; Snaith, H. J.; Thorwart, M.; Li, Z.; et al. Photoinduced Vibrations Drive Ultrafast Structural Distortion in Lead Halide Perovskite. *Journal of the American Chemical Society* **2020**, *142* (39), 16569–16578. DOI: 10.1021/jacs.0c03970.

(82) Batignani, G.; Fumero, G.; Srimath Kandada, A. R.; Cerullo, G.; Gandini, M.; Ferrante, C.; Petrozza, A.; Scopigno, T. Probing femtosecond lattice displacement upon photo-carrier generation in lead halide perovskite. *Nature Communications* **2018**, *9* (1), 1971. DOI: 10.1038/s41467-018-04367-6.

(83) Park, M.; Neukirch, A. J.; Reyes-Lillo, S. E.; Lai, M.; Ellis, S. R.; Dietze, D.; Neaton, J. B.; Yang, P.; Tretiak, S.; Mathies, R. A. Excited-state vibrational dynamics toward the polaron in methylammonium lead iodide perovskite. *Nature Communications* **2018**, *9* (1), 2525. DOI: 10.1038/s41467-018-04946-7.

(84) Monahan, D. M.; Guo, L.; Lin, J.; Dou, L.; Yang, P.; Fleming, G. R. Room-Temperature Coherent Optical Phonon in 2D Electronic Spectra of CH3NH3PbI3 Perovskite as a Possible Cooling Bottleneck. *The Journal of Physical Chemistry Letters* **2017**, *8* (14), 3211–3215. DOI: 10.1021/acs.jpclett.7b01357.

(85) Liu, Z.; Vaswani, C.; Luo, L.; Cheng, D.; Yang, X.; Zhao, X.; Yao, Y.; Song, Z.; Brenes, R.; Kim, R. J. H.; et al. Coherent band-edge oscillations and dynamic longitudinal-optical phonon mode splitting as evidence for polarons in perovskites. *Phys Rev B* **2020**, *101* (11), 115125. DOI: 10.1103/PhysRevB.101.115125.

(86) Lan, Y.; Dringoli, B. J.; Valverde-Chávez, D. A.; Ponseca, C. S.; Sutton, M.; He, Y.; Kanatzidis, M. G.; Cooke, D. G. Ultrafast correlated charge and lattice motion in a hybrid metal halide perovskite. *Science Advances 5* (5), eaaw5558. DOI: 10.1126/sciadv.aaw5558 (accessed 2025/06/14).

(87) Quan, L. N.; Park, Y.; Guo, P.; Gao, M.; Jin, J.; Huang, J.; Copper, J. K.; Schwartzberg, A.; Schaller, R.; Limmer, D. T.; et al. Vibrational relaxation dynamics in layered perovskite quantum wells. *Proceedings of the National Academy of Sciences* **2021**, *118* (25), e2104425118. DOI: 10.1073/pnas.2104425118 (accessed 2025/06/14).

(88) Fu, J.; Li, M.; Solanki, A.; Xu, Q.; Lekina, Y.; Ramesh, S.; Shen, Z. X.; Sum, T. C. Electronic States Modulation by Coherent Optical Phonons in 2D Halide Perovskites. *Advanced Materials* **2021**, *33* (11), 2006233. DOI: https://doi.org/10.1002/adma.202006233 (accessed 2025/06/14).

(89) Rojas-Gatjens, E.; Silva-Acuña, C.; Kandada, A. R. S. Peculiar anharmonicity of Ruddlesden Popper metal halides: temperature-dependent phonon dephasing. *Mater Horizons* **2022**, *9* (1), 492–499, 10.1039/D1MH01010G. DOI: 10.1039/D1MH01010G.

(90) Ni, L.; Huynh, U.; Cheminal, A.; Thomas, T. H.; Shivanna, R.; Hinrichsen, T. F.; Ahmad, S.; Sadhanala, A.; Rao, A. Real-Time Observation of Exciton–Phonon Coupling Dynamics in Self-Assembled Hybrid Perovskite Quantum Wells. *ACS Nano* **2017**, *11* (11), 10834–10843. DOI: 10.1021/acsnano.7b03984.

(91) Zhao, W.; Qin, Z.; Zhang, C.; Wang, G.; Dai, X.; Xiao, M. Coherent exciton-phonon coupling in perovskite semiconductor nanocrystals studied by two-dimensional electronic spectroscopy. *Appl Phys Lett* **2019**, *115* (24), 243101. DOI: 10.1063/1.5130636 (accessed 6/14/2025).

(92) Debnath, T.; Sarker, D.; Huang, H.; Han, Z.-K.; Dey, A.; Polavarapu, L.; Levchenko, S. V.; Feldmann, J. Coherent vibrational dynamics reveals lattice anharmonicity in organic–inorganic halide perovskite nanocrystals. *Nature Communications* **2021**, *12* (1), 2629. DOI: 10.1038/s41467-021-22934-2.

(93) Biswas, S.; Zhao, R.; Alowa, F.; Zacharias, M.; Sharifzadeh, S.; Coker, D. F.; Seferos, D. S.; Scholes, G. D. Exciton polaron formation and hot-carrier relaxation in rigid Dion-Jacobson-type two-dimensional perovskites. *Nat Mater* **2024**, *23* (7), 937–943. DOI: 10.1038/s41563-024-01895-z From NLM PubMed-not-MEDLINE.

(94) Li, Z.; Yan, Y.; Song, M.-S.; Xin, J.-Y.; Wang, H.-Y.; Wang, H.; Wang, Y. Exciton–Phonon Coupling of Chiral One-Dimensional Lead-Free Hybrid Metal Halides at Room Temperature. *The Journal of Physical Chemistry Letters* **2022**, *13* (18), 4073–4081. DOI: 10.1021/acs.jpclett.2c00698.

(95) Yang, H.; Mandal, S.; Li, B.; Ghosh, T. K.; Peterson, J. M.; Guo, P.; Dou, L.; Chen, M.; Huang, L. Slow Dephasing of Coherent Optical Phonons in Two-Dimensional Lead Organic Chalcogenides. *Journal of the American Chemical Society* **2024**, *146* (49), 33928–33936. DOI: 10.1021/jacs.4c12643.

(96) Nonato, A.; Rodríguez-Hernández, J. S.; Abreu, D. S.; Soares, C. C. S.; Gómez, M. A. P.; García-Fernández, A.; Señarís-Rodríguez, M. A.; Andújar, M. S.; Ayala, A. P.; Silva, R. X. d.; et al. Strong Electron–Phonon Coupling and Lattice Dynamics in One-Dimensional [(CH3)2NH2]PbI3 Hybrid Perovskite. *Chemistry of Materials* **2025**, *37* (3), 1013–1026. DOI: 10.1021/acs.chemmater.4c02670.

(97) Han, Y.; Cheng, X.; Cui, B.-B. Factors influencing self-trapped exciton emission of low-dimensional metal halides. *Mater Adv* **2023**, *4* (2), 355–373, 10.1039/D2MA00676F. DOI: 10.1039/D2MA00676F.

(98) de Paula, A. M.; Li, S.; Hou, B.; Vadivel, S.; Teles-Ferreira, D. C.; Iudica, A.; Kabacinski, P.; Hosseini, H.; McArthur, J.; Cerullo, G.; et al. Time-Domain Observation of Ultrafast Self-Trapped Exciton Formation in Lead-Free Double Halide Perovskites. *Journal of the American Chemical Society* **2025**, *147* (32), 28923–28931. DOI: 10.1021/jacs.5c06628.